Electrical ocean conductivity variability from observations and its budget from an ocean state estimate

David Samuel Trossman[1] and Robert Tyler[2]

[1]University of Maryland-College Park
[2]University of Maryland, Baltimore County

November 23, 2022

Abstract

Because spatio-temporal variations in ocean heat content (OHC) are strongly predicted by ocean conductivity content (OCC) over most of the global ocean, we analyze the dynamical budget and behavior of the electrical conductivity of seawater. To perform these analyses, we use an ocean-model state estimate designed to accurately represent long-term variations in ocean properties in a dynamically and kinematically consistent way. We show that this model accurately reproduces the spatio-temporal variations in electrical conductivity seen in satellite-derived and in a seasonal climatology product derived from in-situ data, justifying use of the model data to perform further analyses. An empirical orthogonal function analysis suggests that the vast majority of the variance in OHC and OCC can be explained by similar mechanisms. The electrical conductivity budget's most important term is the temperature forcing tendency term, suggesting that ocean heat uptake is the mechanism responsible for the strong relationship between OCC and OHC.

Electrical ocean conductivity variability from observations and its budget from an ocean state estimate

D. S. Trossman,[1,2,3] R. H. Tyler[4,5]

[1]Earth System Science Interdisciplinary Center, University of Maryland, College Park, MD, USA
[2]Department of Oceanography and Coastal Sciences, Louisiana State University, Baton Rouge, LA, USA
[3]Center for Computation & Technology, Louisiana State University, Baton Rouge, LA, USA
[4]Geodesy and Geophysics Laboratory, Code 61A, NASA Goddard Space Flight Center, Greenbelt, MD, USA
[5]Goddard Earth Science and Technology Research (GESTAR) II, University of Maryland, Baltimore County, MD, USA

Key Points:

- Close agreement between observationally-derived and ECCO-calculated conductivity
- Temperature forcing tendency term dominates electrical conductivity budget
- Conductivity can be locally influenced by advection of temperature (low-latitudes) and salinity (high-latitudes)

Corresponding author: David S. Trossman, david.s.trossman@gmail.com

Abstract

Because spatio-temporal variations in ocean heat content (OHC) are strongly predicted by ocean conductivity content (OCC) over most of the global ocean, we analyze the dynamical budget and behavior of the electrical conductivity of seawater. To perform these analyses, we use an ocean-model state estimate designed to accurately represent long-term variations in ocean properties in a dynamically and kinematically consistent way. We show that this model accurately reproduces the spatio-temporal variations in electrical conductivity seen in satellite-derived and in a seasonal climatology product derived from in-situ data, justifying use of the model data to perform further analyses. An empirical orthogonal function analysis suggests that the vast majority of the variance in OHC and OCC can be explained by similar mechanisms. The electrical conductivity budget's most important term is the temperature forcing tendency term, suggesting that ocean heat uptake is the mechanism responsible for the strong relationship between OCC and OHC.

Plain Language Summary

The ocean conducts electricity because it contains charged particles. While the dynamical budget and behavior of ocean temperature and salinity have been well studied, similar basic analyses have not been conducted for ocean conductivity. The goal of this study is to provide this using realistic ocean conductivity data describing spatial and temporal variations. Providing a realistic description of conductivity and its dynamical variability is motivated by recent interest in using in-situ and remote estimates of ocean conductivity content (OCC) to infer ocean heat content (OHC). The latter is both highly important in understanding climate change and inadequately observed using traditional methods. The primary result of this study is that, in most of the global ocean, both spatial and temporal variability in OHC are strongly predicted by OCC through ocean heat uptake, raising the importance of developing electric and magnetic methods for monitoring OCC and thereby OHC by proxy.

1 Introduction

While electrical conductivity is a fundamental parameter in the electrodynamics of the ocean, in the more typical fields of physical oceanography treating fluid dynamics and thermodynamics, electrical conductivity is usually only discussed as a proximate variable for conveniently obtaining salinity. Conductivity is indeed much easier to measure than salinity directly. In fact, ocean salinity has become defined by referencing observations of electrical conductivity of a seawater sample to that of a potassium chloride solution under standardized temperature and pressure conditions [*UNESCO*, 1985]. At given pressure, the electrical conductivity of the ocean alone does not provide sufficient information to associate it with a unique combination of temperature and salinity. However, given two of the three (electrical conductivity, temperature, and salinity), the third can be uniquely determined, despite their nonlinear relationship.

Because salinity is required to estimate the dynamically important density, conductivity has been extensively measured in the ocean to high accuracy. However, the conductivity data itself has not typically been archived. Rather, it must be estimated from the archived temperature and salinity co-observations. This approach was followed in developing the first 'climatology' data set for ocean conductivity [*Tyler et al.*, 2017], which has since been updated in *Reagan et al.* [2019]. Climatology data sets (long available for temperature and salinity) refer to gridded data products constructed from an objective analysis of the many observations. The latest WOA18 data in *Reagan et al.* [2019] provides global ocean conductivity at 0.25-degree (latitude and longitude) resolution and 102 standard levels spanning the ocean depth. This data includes sets (used in the present study) describing the temporal mean as well as each of four seasons. Further, satellite-derived sea surface temperature and salinity observations provide some information about the interannual variability in sea surface conductivity.

While conductivity depends on both temperature and salinity, an interesting finding in the climatology data [*Tyler et al.*, 2017] was that the depth average of conductivity is strongly related to that of temperature, motivating further studies which have found support for using depth-integrated conductivity ("conductance" or, as shall be referred to here, "ocean conductivity content" (OCC)) to predict depth-integrated heat ("ocean heat content" (OHC)) [*Trossman and Tyler*, 2019; *Irrgang et al.*, 2019; *Trossman and Tyler*, 2022]. Of course depth-integrated parameters can show strong spatial co-variability simply due to the common depth and the relationships referred to here involve either depth-averaged variables or covariability beyond what can be simply explained by depth. The goal of the present study is to describe conductivity data sets that contain realistic spatial and temporal variability and apply this for elucidating the dynamical reasons for the high covariability between OCC and OHC.

A second reason for describing the realistic behavior of ocean conductivity is that this data is needed in forward models of ocean electrodynamics. The ocean is permeated by large-scale electric currents generated by induction (involving excitation by field sources in the ionosphere and magnetosphere; e.g., *Kuvshinov* [2008]) and motional induction (due to the motion of the electrically conducting fluid, such as the ocean, through the Earth's main magnetic field), which have associated local and remote magnetic fields (e.g., [*Sanford*, 1971; *Stephenson and Bryan*, 1992; *Tyler et al.*, 1997; *Manoj et al.*, 2006]). Because the ocean is electrically thin for periods longer than about 10 minutes [*Tyler*, 2017], the horizontal electric currents associated with the ocean's remotely-observable magnetic fields pass through the whole water column, with the result that the ocean's magnetic fields are modulated by depth-integrated electrical conductivity (OCC) rather than surface electrical conductivity. However, due to the insufficient spatio-temporal sampling of the full-depth observations of electrical conductivity, our knowledge of the interannual variability in the subsurface ocean's electrical conductivity is lacking, which is one focus of the present study.

No previous study has balanced a tracer tendency equation for the ocean's electrical conductivity, in which each physical factor impacting the electrical conductivity has its time-rate of change quantified and balanced with the total time derivative (referred to as a "budget" hereafter). However, there are numerous studies that have evaluated these types of budgets for ocean heat, salt, and (steric) sea level. For example, using an observationally-constrained but dynamically and kinematically consistent ocean state estimate, *Piecuch and Ponte* [2011] showed that the interannual variations in sea level are primarily associated with steric sea level and that variations in steric sea level are mostly due to advection in the tropical Indian and Pacific oceans and both advection and diffusion at extratropical latitudes, with local surface buoyancy fluxes contributing in relatively few regions. Using a free-running coupled climate model, *Palter et al.* [2014] found diffusion to be more important to steric sea level variability on a global-mean scale than *Piecuch and Ponte* [2011], at least when considering vertical versus lateral diffusion separately, but their results otherwise qualitatively agree. *Piecuch and Ponte* [2014] further demonstrated that the global-mean steric sea level trend is set by surface heat and freshwater exchanges that are primarily offset by the redistribution of heat and salt through advection and diffusion, which generally agrees with the results of *Palter et al.* [2014]. The relative roles of temperature and salinity variability associated with different physical processes in determining the electrical conductivity variability remain unknown.

The modeling system used to generate the electrical conductivity budget data analyzed here (a run of the Estimating the Circulation & Climate of the Ocean (ECCO) framework [*Fukumori et al.*, 2017] from 1992 to 2015 without having to optimize the model's free parameters again, a "re-run") is described in the following section. Essentially, the optimized run of ECCO solves for the initial conditions, model parameters, and forcing fields using an adjoint-based data assimilation method. These estimates are then utilized in a forward simulation (the re-run) with new diagnostics (e.g., each tendency term in the electrical conductivity budget, broken up by temperature and salinity contributions) saved as model output. There are at least three strengths in using ECCO to assess whether OHC can be predicted from OCC. First, model output is more globally complete than observational datasets in both time and space. Second, ECCO has been validated against several independent data sets [*Forget et al.*, 2015a; *Heimbach et al.*, 2019]. Third, its re-run is guaranteed to maintain consistency in the dynamics and physics of its underlying ocean model, which filter-based reanalyses cannot do due to their use of analysis increments [*Stammer et al.*, 2016; *Pilo et al.*, 2018].

In this study, we consider how advection, diffusion, and forcings of heat and salt determine the variability in electrical conductivity using a more updated version of the same ocean state estimation framework as *Piecuch and Ponte* [2011]. We organize this manuscript as follows. In the Supplementary Information, we describe the observations with which we use to assess how realistic the ECCO state estimate's output is and the observation-model comparisons. In the main text, we describe ECCO and the conductivity budget. We then describe the analysis of what explains the variability in depth-integrated electrical conductivity and other correlates, and the electrical conductivity budget results. We lastly make concluding remarks for the consequences of our findings and for future research.

2 Model description and budget framework

2.1 Modeling system

The modeling system used here is the ECCO-Production version 4 revision 3 (ECCO-Production ver4.rev3 or ECCOv4r3) run, which was accomplished and described by *Fukumori et al.* [2017]. The same framework was used by *Trossman and Tyler* [2019, 2022], but is described again here. The underlying ocean-sea ice model for ECCOv4r3 is based on the Massachusetts Institute of Technology general circulation model (MITgcm), which is a global finite volume model. The ECCOv4r3 global configuration uses curvilinear Cartesian coordinates (*Forget et al.* [2015a] - see their Figs. 1-3) at a nominal 1^o (0.4^o at equator) resolution and rescaled height coordinates [*Adcroft and Campin*, 2004] with 50 vertical levels and a partial cell representation of bottom topography [*Adcroft et al.*, 1997]. The MITgcm uses a dynamic/thermodynamic sea ice component [*Menemenlis et al.*, 2005; *Losch et al.*, 2010; *Heimbach et al.*, 2010] and a nonlinear free surface with freshwater flux boundary conditions [*Campin et al.*, 2004]. The wind speed and wind stress are specified as 6-hourly varying input fields over 24 years (1992-2015). Average adjustments to the wind stress, wind speed, specific humidity, shortwave downwelling radiation, and surface air temperature are re-estimated and then applied over 14-day periods. These adjustments are based on estimated prior uncertainties for the chosen atmospheric reanalysis [*Chaudhuri et al.*, 2013], which is ERA-Interim [*Dee et al.*, 2011]. The net heat flux is then computed via a bulk formula [*Large and Yeager*, 2009]. The ocean variables, on the other hand, do not get periodically adjusted. A parameterization of the effects of geostrophic eddies [*Gent and McWilliams*, 1990] is used. Mixing along isopycnals is accounted for according to the framework provided by *Redi* [1982]. Vertical mixing is the sum of diapycnal mixing and the vertical component of the along-isopycnal tensor, where diapycnal mixing is determined according to the *Gaspar et al.* [1990] mixed layer turbulence closure and estimated background diapycnal diffusivity. Convective adjustment does not act through the diapycnal diffusivity in the MITgcm. Here, the model's diapycnal diffusivity represents a combination of processes, including–but potentially not limited to–internal wave-induced mixing. The background diapycnal diffusivity, the Redi coefficient, and the Gent-McWilliams coefficient are time-independent because of the under-determined problem of inverting for initial conditions and model parameters would be even more under-determined if they were allowed to vary in time. The electrical conductivity is calculated using the TEOS-10 package [*MacDougall and Barker*, 2011] as the model runs by solving for the in-situ temperature based on the simulated potential temperature.

The objective of the optimized ECCOv4r3 solution is to minimize the cost function, which is a combination of 1) a weighted sum of squares of the disagreements between the model and observations and 2) a sum of penalties that do not appear in the estimation itself but push control variables towards certain parts of the control space. The least-squares problem solved by the ECCO model uses the method of Lagrange multipliers through iterative improvement, which relies upon a quasi-Newton gradient search [*Nocedal*, 1980; *Gilbert and Lemarechal*, 1989]. Algorithmic (or automatic) differentiation tools [*Griewank*, 1992; *Giering and Kaminski*, 1998] have allowed for the practical use of Lagrange multipliers in a time-varying non-linear inverse problem such as ocean modeling, eliminating the need for discretized adjoint equations to be explicitly hand-coded. Contributions of observations to the model-data misfit function are weighted by best-available estimated data and model representation error variance [*Wunsch and Heimbach*, 2007]. The observational data included in the ECCO state estimation procedure are discussed in *Forget et al.* [2015a] and *Fukumori et al.* [2017]. These data include satellite-derived ocean bottom pressure anomalies, sea ice concentrations, sea surface temperatures, sea surface salinities, sea surface height anomalies, and mean dynamic topography, as well as profiler- and mooring-derived temperatures and salinities [*Fukumori et al.*, 2017] (see their Table 3). The control variables that are inverted for iteratively by ECCO include the initial condition of the velocities, sea surface heights, temperatures, and salinities; time-mean three-dimensional Redi [*Redi*, 1982] coefficients, Gent-McWilliams *Gent and McWilliams* [1990] coefficients, and vertical diffusivities [*Gaspar et al.*, 1990]; and time-varying two-dimensional surface forcing fields. The error covariances for each of the ocean subgrid-scale transport and mixing parameters are specified by imposing a smoothness operator [*Weaver and Courtier*, 2001] at the scale of three grid points–decorrelation length scale diameter of $\sim$ 100 km–which allows for the dynamical model to regionally adjust from the information provided by observations [*Forget et al.*, 2015b]. Fifty-nine iterations of the parameter and state estimation procedure–the "optimization" run–were performed to arrive at the ECCOv4r3 solution, which we use for initial conditions and model parameters in our experiments.

2.2 Electrical conductivity budget

In order to examine the importance of particular processes to variations in electrical conductivity (σ) we analyze a modified version of ECCOv4r3's temperature and salinity budgets to calculate the electrical conductivity budget. In order words, we calculate the instantaneous time-rate of change in electrical conductivity, $\partial\sigma/\partial t$, and each physical process that affects the electrical conductivity (their "tendencies") for each model time step. The tracer tendency equation terms required for the potential temperature (Θ) budget are related to those for the electrical conductivity budget by multiplying by $\partial\sigma/\partial\Theta$ and the tracer tendency equation terms required for the salinity (S) budget are related to those for the electrical conductivity budget by multiplying by $\partial\sigma/\partial S$. Each of these terms are computed online and saved as the model runs. That is, we compute the terms in the electrical conductivity budget inline before saving them as model output instead of calculating these fields offline from averaged model output of tendencies in temperature and salinity because the chain rule is applied to get tendencies in electrical conductivity. Finally, the monthly averages of the resulting electrical conductivity tendencies are saved to the output files used in this analysis.

The tracer equations can be broken down into individual contributions [*Palter et al.*, 2014],

$$\begin{aligned} \rho\frac{d\Theta}{dt} &= -\nabla\cdot\mathbf{J}^{\Theta} + \rho Q^{\Theta} \\ \rho\frac{dS}{dt} &= -\nabla\cdot\mathbf{J}^{S} + \rho Q^{S}, \end{aligned} \tag{1}$$

where $d/dt = \partial/\partial t + (\mathbf{v}+\mathbf{v}^{*})\cdot\nabla$ is the material derivative, $\mathbf{v}$ is the resolved velocity field, $\mathbf{v}^{*}$ is the eddy-induced or quasi-Stokes velocity field that represents parameterized motions, Θ is the potential temperature, S is the salinity, ρ is the locally referenced potential density,

$\mathbf{J}^{\Theta}$ and $\mathbf{J}^{S}$ are the parameterized along-isopycnal and diapycnal mixing fluxes associated with potential temperature and salinity, and Q^{Θ} and Q^{S} are the sums of sources and sinks of potential temperature and salinity.

The potential temperature and salinity budget terms summarized by Equation (1) are computed as follows. The resolved and mesoscale transports are accounted for in the material derivatives Θ and S, and the along-isopycnal and diapycnal diffusion of Θ and S are accounted for by $\mathbf{J}^{\Theta}$ and $\mathbf{J}^{S}$. The diapycnal diffusion term is added to the vertical component of the along-isopycnal diffusion term, which is against convention (e.g., *Palter et al.* [2014]). Shortwave radiation flux is allowed to penetrate down to 200 m in an exponentially decaying manner [*Paulson and Simpson*, 1977]. The sources and sinks of Θ and S accounted for by Q^{Θ} and Q^{S} include surface buoyancy fluxes (latent, sensible, shortwave, longwave, and frazil heat fluxes); geothermal heat flux; precipitation minus evaporation; freshwater fluxes from land ice; and frazil ice formation.

3 Results

The high level of agreement between ECCOv4r3 and observations (see Supplementary Information; Figs. S1-S2) justifies using the ECCOv4r3 data for the remainder of this study. Unlike the observational comparisons, when we refer to OCC, OHC, and OSC, hereafter, we are referring to full depth-integrated quantities. We present the temporally averaged OCC, its spatial gradients, and depth-averaged equivalents (Fig. S3) and their temporal variability (Fig. S4) over the length of the ECCOv4r3 simulation (1992-2015) in the Supplementary Information for reference.

3.1 Covariability of OCC, OHC, and OSC in ECCOv4r3

Using the ECCOv4r3 output from our new simulations, we investigate the covariability between OCC, OHC, and OSC. We perform an empirical orthogonal function (EOF) decomposition of each field after removing each of their means (Fig. 1) and extend this to a multivariate EOF (MEOF) analysis in the Supplementary Information to demonstrate the spatial patterns of covariability in OCC and OHC (Fig. S5). We area-weight each field and normalize them by their standard deviations prior to calculating the EOFs. The first EOF for OHC and the first EOF for OCC are related to ocean warming (Figs. 1a-b) and explain between one-third and one-half of each of their variances. The first EOF for OSC is related to land ice melt (Fig. 1c) and explains 60% of the variance. The second EOF for OHC and the second EOF for OCC are related to natural climate variability (Figs. 1d-e) such as the El Niño Southern Oscillation, consistent with previous analyses that used observations of only the upper 700 meters (e.g., *Wang et al.* [2020]). The second EOF for OSC is related to sea ice melt and evaporation minus precipitation trends (Fig. 1f). While the OCC, OHC, and OSC tend to be highly correlated regardless of season and it is unclear whether any EOF beyond the second has a physical interpretation (not shown), the first several EOFs for OHC and OCC are significantly correlated in space (Fig. 1g), whereas only the first EOF for OSC and OCC are significantly correlated in space (Fig. 1h). The maximum and minimum bootstrapped spatial correlations are shown in Figs. 1g-h (red dashed curves) around their averages (solid green curves) in comparison to maximum canonical spatial correlations (solid black curves) to indicate which EOFs are significantly correlated. Consistent with the low predictability of OHC from OCC on seasonal time scales found by *Trossman and Tyler* [2022], only the first several EOFs for OCC and OHC highly correlate when a filter is not applied, but the vast majority of EOFs for OCC and OHC highly correlate when a year-long moving average filter is applied to the OCC and OHC data (Fig. 1g). Thus, it is likely that the same mechanisms that explain the variability in OHC can also explain the annual-to-longer-term variability in OCC. We investigate this further below.

3.2 Conductivity budget analysis

We next decompose the electrical conductivity budget into contributions from temperature and salinity and for each of those, the depth-average of the horizontal advection, vertical advection, horizontal diffusion, vertical diffusion, forcing, and total tendency terms are shown in Fig 2. Regionally, there are large differences between the magnitudes of the temperature and salinity contributions for a given advective, diffusive, or forcing term. The temperature forcing term tends to dominate not only the salinity forcing term but every other term in the electrical conductivity budget. However, the redistribution of electrical conductivity (or its transport) is primarily determined by the advection of both temperature and salinity. Salinity's advective contributions are larger than temperature's advective contributions in high-latitude regions and temperature's advective contributions are larger than salinity's advective contributions in low-latitude regions. The vertical advection contributions tend to be of opposite sign from the horizontal advection contributions, with the exception of salinity's advective contributions in equatorial regions. The sign is actually opposite between temperature's horizontal diffusion contributions and the salinity's horizontal diffusion contributions in equatorial regions. The total tendency term for temperature is primarily determined by the temperature forcing term and the total tendency term for salinity is mostly set by salinity's horizontal advection term, with a net non-zero tendency when you add these two tendency terms together because there is a trend in ECCO's electrical conductivity.

We lastly present the electrical conductivity budget tendency terms in Fig. 3. We first focus on the zonally- and depth-averaged tendencies (Fig. 3a). The temperature forcing term tracks the total temperature tendency term very closely over all latitudes. The temperature forcing, vertical advection of salinity, and horizontal advection of temperature contributions to the electrical conductivity dominate but are slightly offset by vertical diffusion of salinity near Antarctica. There is a trade-off of temperature forcing, vertical advection of temperature, and horizontal advection of temperature in low-latitude regions. In subpolar regions of the Northern Hemisphere, temperature forcing and vertical advection of salinity are partially offset by horizontal advection of salinity. All other terms are relatively small in their zonal and depth averages, but the diffusion terms may be underestimated, as suggested by *Trossman et al.* [2022]. The temporal variations in the tendency terms are primarily seasonal with amplitudes that can be larger than the average tendencies for many terms (Fig. 3b). The temperature and salinity advection tendency terms, particularly temperature's horizontal advection term, can be comparable in magnitude to the temperature forcing tendency term during July-September. The area-weighted global averages of the temporal correlations between each tendency term and the total tendencies (Table 1) reveal that only the temperature forcing tendency term is significantly positively correlated with the total electrical conductivity tendency term, but the vertical advection of salinity term is marginally anti-correlated with the total electrical conductivity tendency term, suggesting a redistributive role. The temporal correlations between the temperature forcing tendency term and the total tendency term are lower in the Arctic Ocean, consistent with lower predictability of OHC from OCC and other factors found by *Trossman and Tyler* [2022]. Each term can be significantly correlated with the total tendency at some location in the ocean. However, the only field with both significant temporal correlations with the total tendency term (Table 1) and a non-negligible global area-weighted tendency (Fig. 3b) is the temperature forcing tendency term. These findings suggest that the electrical conductivity tendencies are primarily determined by ocean heat uptake, which is consistent with the high correlation between OCC and OHC found by *Trossman and Tyler* [2019, 2022] given that ocean heat uptake is mostly passively advected and diffused globally, particularly outside of the Atlantic Ocean [*Garuba and Klinger*, 2018; *Zika et al.*, 2021].

4 Conclusions

In the present study, we investigated the reasons for the high level of full-depth ocean heat content (OHC) predictability from full-depth ocean conductivity content (OCC) *Tross-*

man and Tyler [2019, 2022] that could potentially be calculated from magnetic data. We used an ocean state estimate (ECCO) to perform this analysis, which we justified by assessing its agreement with two different observational products (one from satellites and one from in-situ data – see Supplementary Information). We performed multiple calculations to assess the covariability between OHC and (with an EOF analysis) and to ascribe causality to specific processes (with an electrical conductivity budget analysis).

This study provided a first long-term assessment of sea surface electrical conductivity statistics using satellite data and found good agreement with the ECCOv4r3 product. Consistent with the high level of agreement with in-situ temperature and salinity observations summarized by *Heimbach et al.* [2019], we found good agreement between the electrical conductivity from ECCOv4r3 and in-situ observations on a seasonal time scale. However, the agreement between ECCOv4r3 and in-situ observations degrades at deeper depths and is relatively worse below 2000 meters depth in high-latitude regions.

Lastly, we investigated why OCC and OHC are so strongly related to each other. We first demonstrated that the near-surface conductivity predominates the variability in OCC and near-surface velocities determine the variability in the horizontal gradients in OCC. We then performed EOF and electrical conductivity budget analyses. The EOF analysis suggested that the drivers of the vast majority of the variance in the OHC and OCC fields from ECCOv4r3 are similar. We further found that the temperature forcing tendency dominates the electrical conductivity budget, but the advection tendency terms can be important locally and at particular times of the year. These results suggest that the main reason why the OHC (anomaly) is highly predictable from the OCC (anomaly) is that ocean heat uptake is primarily driving the trends in electrical conductivity. This study suggests that developing the capability to monitor OCC using available observing systems (e.g., satellite magnetometry and land observatories) would be beneficial to ocean heat content monitoring efforts.

Acknowledgments

The authors are grateful for the sea surface conductivity data generated by James Reagan. David S. Trossman and Robert H. Tyler were supported by the National Science Foundation, Directorate for Geosciences, OCE-2048789. The authors acknowledge the Texas Advanced Computing Center (TACC) at The University of Texas-Austin for providing HPC resources that have contributed to the research results reported within this paper

(URL: http://www.tacc.utexas.edu). The data used in this study can be found at: https://doi.org/10.5281/zenodo.6834064

References

Adcroft, A., C. Hill, J. Marshall (1997), The representation of topography by shaved cells in a height coordinate model, *Mon. Wea. Rev.*, **125**, 2293—2315.

Adcroft, A., J.-M. Campin (2004), Rescaled height coordinates for accurate representation of free-surface flows in ocean circulation models, *Ocean Modelling*, **7**, 269—284.

Campin, J.-M., A. Adcroft, C. Hill, J. Marshall (2004), Conservation of properties in a free surface model, *Ocean Modelling*, **6**, 221—244.

Chaudhuri, A. H., R. M. Ponte, G. Forget, P. Heimbach (2013), A comparison of atmospheric reanalysis surface products over the ocean and implications for uncertainties in air-sea boundary forcing, *J. Clim.*, **26**, 153—170.

Dee, D. P., S. M. Uppala, A. J. Simmons, P. Berrisford, P. Poli S. Kobayashi U. Andrae M. A. Balmaseda G. Balsamo P. Bauer P. Bechtold A. C. M. Beljaars L. van de Berg J. Bidlot N. Bormann C. Delsol R. Dragani M. Fuentes A. J. Geer L. Haimberger S. B. Healy H. Hersbach E. V. Hólm L. Isaksen P. Kållberg M. Köhler M. Matricardi A. P. McNally B. M. Monge-Sanz J.-J. Morcrette B.-K. Park C. Peubey P. de Rosnay C. Tavolato J.-N. Thépaut F. Vitart (2011), The ERA-Interim reanalysis: configuration and performance of the data assimilation system, *Q. J. Royal Met. Soc.*, **137**, 553—597.

Ferrari, R., J. C. McWilliams, V. M. Canuto, M. Dubovikov, (2008), Parameterization of eddy fluxes near oceanic boundaries. *J. Climate*, **21**, 2770–2789.

Ferrari, R., S. M. Griffies, A. J. G. Nurser, G. K. Vallis, (2010), A boundary-value problem for the parameterized mesoscale eddy transport. *Ocean Model.*, **32**, 143–156.

Forget, G., J.-M. Campin, P. Heimbach, C. N. Hill, R. M. Ponte, C. Wunsch (2015a), ECCO version 4: an integrated framework for nonlinear inverse modeling and global ocean state estimation, *Geosci. Model Dev.*, **8**(10), 3071—3104, doi:10.5194/gmd-8-3071-2015; http://www.geosci-model-dev.net/8/3071/2015/.

Forget, G., D. Ferreira, X. Liang, (2015b), On the observability of turbulent transport rates by Argo: supporting evidence from an inversion experiment. *Ocean Sci.*, **11**, 839–853, https://doi.org/10.5194/os-11-839-2015.

Fukumori, I., O. Wang, I. Fenty, G. Forget, P. Heimbach, R. M. Ponte (2017), ECCO Version 4 Release 3, DSpace@MIT, http://hdl.handle.net/1721.1/110380.

Garuba, O. A., B. A. Klinger (2018), Ocean Heat Uptake and Interbasin Transport of the Passive and Redistributive Components of Surface Heating. *Journal of Climate*, **29**(20), 7507–7527; https://doi.org/10.1175/JCLI-D-16-0138.1

Gaspar, P., Y. Grégoris, J.-M. LeFevre (1990), A simple eddy kinetic energy model for simulations of the oceanic vertical mixing: tests at Station Papa and long-term upper ocean study site, *J. Geophys. Res.*, **95**, 16,179—16,193.

Gent, P. R., J. C. McWilliams (1990), Isopycnal mixing in ocean circulation models, *J. Phys. Oceanogr.*, **20**, 150—155.

Gerdes, R., C. K oberle, J. Willebrand, (1990), The influence of numerical advection schemes on the results of ocean general circulation models. *Clim. Dynam.*, **5**, 211–226.

Gilbert, J. C., C. Lemarechal (1989), Some numerical experiments with variable-storage quasi-Newton algorithms, *Math. Program.*, **45**, 407—435.

Giering, R., T. Kaminski (1998), Recipes for adjoint code construction, *ACM Transactions on Mathematical Software*, **24**, 437—474.

Grayver, A. V. (2021), Global 3-D electrical conductivity model of the world ocean and marine sediments, *Geochemistry, Geophysics, Geosystems*, **22**, e2021GC009950, https://doi.org/10.1029/2021GC009950

Griewank, A. (1992), Achieving logarithmic growth of temporal and spatial complexity in reverse automatic differentiation, *Optimization Methods and Software*, **1**:1, 35—54, doi:10.1080/10556789208805505

Heimbach, P., D. Menemenlis, M. Losch, J. M. Campin, C. Hill (2010), On the formulation of sea-ice models. Part 2: Lessons from multi-year adjoint sea ice export sensitivities through the Canadian Arctic Archipelago, *Ocean Modelling*, **33**, 145—158, doi:10.1016/j.ocemod.2010.02.002.

Heimbach, P., I. Fukumori, C. N. Hill, R. M. Ponte, D. Stammer, C. Wunsch, J.-M. Campin, B. Cornuelle, I. Fenty, G. Forget, A. K ohl, M. Mazloff, D. Menemenlis, A. T. Nguyen, C. Piecuch, D. Trossman, A. Verdy, O. Wang, H. Zhang (2019), Putting it all together: Adding value to the global ocean and climate observing systems with complete self-consistent ocean state and parameter estimates, *Frontiers in Marine Science*, **6**:55, doi:10.3389/fmars.2019.00055.

Irrgang, C., J. Saynisch, M. Thomas (2017), Utilizing oceanic electromagnetic induction to constrain an ocean general circulation model: A data assimilation twin experiment, *Journal of Advances in Modeling Earth Systems*, **9**, 1703—1720, https://doi.org/10.1002/2017MS000951

Irrgang, C., J. Saynisch, M. Thomas (2019), Estimating global ocean heat content from tidal magnetic satellite observations, *Nature Sci. Rep.*, **9**:7893, https://doi.org/10.1038/s41598-019-44397-8.

Kuvshinov, A. V. (2008). 3-D global induction in the oceans and solid Earth: Recent progress in modeling magnetic and electric fields from sources of magnetospheric, ionospheric and oceanic origin. *Surveys in Geophysics*, **29**, 139–186.

Large, W. G., S. G. Yeager, (2009), The global climatology of an interannually varying air-sea flux data set. *Clim. Dynam.*, **33**, 341–364.

Losch, M., D. Menemenlis, J. M. Campin, P. Heimbach, C. Hill, 2010: On the formulation of sea-ice models. Part 1: Effects of different solver implementations and parameterizations. *Ocean Modelling*, **33**, 129—144, doi:10.1016/j.ocemod.2009.12.008.

McDougall, T. J., P. M. Barker, 2011: Getting started with TEOS-10 and the Gibbs Seawater (GSW) Oceanographic Toolbox, 28pp., SCOR/IAPSO WG127, ISBN 978-0-646-55621-5.

Manoj, C., A. Kuvshinov, S. Maus, H. Luhr, (2006), Ocean circulation generated magnetic signals. *Earth, Planets and Space*, **58**(4), 429–437.

Manoj, C., A. Kuvshinov, S. Neetu, T. Harinarayana (2010), Can undersea voltage measurements detect tsunamis? *Earth, Planets and Space*, **62**, 353—358.

Menemenlis, D., and Coauthors, 2005: NASA supercomputer improves prospects for ocean climate research. *Eos, Trans. Amer. Geophys. Union*, **86**, 95—96.

Minami, T., H. Toh, R. H. Tyler, 2015: Properties of electromagnetic fields generated by tsunami first arrivals: Classification based on the ocean depth. *Geophysical Research Letters*. http://doi.org/10.1002/2015GL063055/pdf

Minami, T., 2017: Motional Induction by Tsunamis and Ocean Tides: 10 Years of Progress. *Surveys in Geophysics*, 1–36. http://doi.org/10.1007/s10712-017-9417-3

Nocedal, J. (1980), Updating quasi-Newton matrices with limited storage, *Mathematics of Computation*, **35**(151), 773—782.

Palter, J. B., S. M. Griffies, B. L. Samuels, E. D. Galbraith, A. Gnanadesikan, A. Klocker (2014), The deep ocean buoyancy budget and its temporal variability, *J. Clim.*, **27**, 551—573.

Paulson, C. A., J. J. Simpson, 1977: Irradiance Measurements in the Upper Ocean. *J. Phys. Oceanogr.*, **7**, 952–956.

Petereit, J., J. Saynisch-Wagner, C. Irrgang, M. Thomas, 2019: Analysis of ocean tide-induced magnetic fields derived from oceanic in situ observations: Climate trends and the remarkable sensitivity of shelf regions. *Journal of Geophysical Research-Oceans*, **124**, 8257—8270. https://doi.org/10.1029/2018JC014768

Piecuch, C. G., R. M. Ponte (2011), Mechanisms of interannual steric sea level variability, *Geophys. Res. Lett.*, **38**, L15605, doi:10.1029/2011GL048440.

Piecuch, C. G., R. M. Ponte (2014), Mechanisms of global-mean steric sea level change, *J. Clim.*, **27**, 824—834.

Pilo, G. S., P. R. Oke, R. Coleman, T. Rykova, K. Ridgway, (2018), Impact of data assimilation on vertical velocities in an eddy resolving ocean model. *Ocean Model.*, **131**, 71–85.

Ponte, R. M., K. J. Quinn, C. Wunsch, P. Heimbach (2007), A comparison of model and GRACE estimates of the large-scale seasonal cycle in ocean bottom pressure, *Geophys.*

Res. Lett., **34**, L09603, doi:10.1029/2007GL029599.

Reagan, J.R., M.M. Zweng, D. Seidov, T.P. Boyer, R.A. Locarnini, A.V. Mishonov, O.K. Baranova, H.E. Garcia, K.W. Weathers, C.R. Paver, I.V. Smolyar, R.H. Tyler (2019). World Ocean Atlas 2018, Volume 6: Conductivity. A. Mishonov Technical Editor, NOAA Atlas NESDIS 86, 38 pp.

Redi, M. H. (1982), Oceanic isopycnal mixing by coordinate rotation, *J. Phys. Oceanogr.*, **12**, 1154—1158.

Sabaka, T. J., R. H. Tyler, N. Olsen, A. Kuvshinov, 2015: CM5, a pre-Swarm comprehensive geomagnetic field model derived from over 12yr of CHAMP, rsted, SAC-C and observatory data. *Geophysical Journal International*, **200**(3), 1596—1626. doi: 10.1093/gji/ggu493

Sabaka, T. J., R. H. Tyler, R. H., N. Olsen, 2016: Extracting ocean-generated tidal magnetic signals from Swarm data through satellite gradiometry. *Geophysical Research Letters*, **43**(7), 3237—3245.

Sabaka, T. J., L. Tøffner-Clausen, N. Olsen, C. C. Finlay, 2018: A comprehensive model of Earth's magnetic field determined from 4 years of Swarm satellite observations. *Earth, Planets and Space*, **70**(1), 130. doi: 10.1186/s40623-018-0896-3

Sanford, T. B., 1971: Motionally induced electric and magnetic fields in the sea. *Journal of Geophysical Research*, **76**, https://doi.org/10.1029/JC076i015p03476, http://www.agu.org/pubs/crossref/1971/JC076i015p03476.shtml.

Schnepf , N. R., M. C. Nair, J. Velímský, N. P. Thomas, 2020: Can seafloor voltage cables be used to study large-scale circulation? An investigation in the Pacific Ocean. *Ocean Sci. Disc.*, https://doi.org/10.5194/os-2019-129

Stammer, D., M. Balmaseda, P. Heimbach, A. Köhl, A. Weaver, 2016: Ocean data assimilation in support of climate applications: status and perspectives. *Annu. Rev. Mar. Sci.*, **8**, 491—518, 10.1146/annurev-marine-122414-034113.

Stephenson, D., K. Bryan, (1992), Large-scale electric and magnetic fields generated by the oceans. *Journal of Geophysical Research*, **97**(C10), 15467.

Treguier, A. M., (1992), Kinetic energy analysis of an eddy resolving, primitive equation model of the North Atlantic. *J. Geophys. Res.*, **97**, 687–701.

Trossman, D. S., R. H. Tyler, 2022: A Prototype for Remote Monitoring of Ocean Heat Content Anomalies. *Journal of Atmospheric and Oceanic Technology*, **39**(5), 667–688; https://doi.org/10.1175/JTECH-D-21-0037.1

Trossman, D. S., R. H. Tyler, 2019: Predictability of Ocean Heat Content from Electrical OCC. *Journal of Geophysical Research-Oceans*, **124**, 667-679; https://doi.org/10.1029/2018JC014740.

Trossman, D. S., C. Whalen, T. W. N. Haine, A. F. Waterhouse, A. Bigdeli, A. T. Nguyen, M. Mazloff, P. Heimbach, 2022: Tracer and Observationally Derived Constraints on Diapycnal Diffusivities in an Ocean State Estimate. *Ocean Science*, **18**, 729–759; https://doi.org/10.5194/os-18-729-2022.

Tyler, R., L. Mysak, 1995: Electrodynamics in a rotating frame of reference with application to global ocean circulation. *Canadian Journal Physics*, **73**(5-6), 393–402.

Tyler, R. H., T. B. Sanford, J. M. Oberhuber, (1997), Geophysical challenges in using large-scale ocean-generated EM fields to determine the ocean flow. *Journal Geomagnetism and Geoelectricity*, **49**(11–12), 1351–1372.

Tyler, R. H., S. Maus, H. L uhr, 2003: Satellite observations of magnetic fields due to ocean tidal flow. *Science*, **299**(5604), 239—241.

Tyler, R., 2005: A simple formula for estimating the magnetic fields generated by tsunami flow. *Geophysical Research Letters*, **32**(9), L09608.

Tyler, R., T. J. Sabaka, 2016: Magnetic remote sensing of ocean heat content. *AGU Fall Meeting Abstracts*, GC31D-1142, https://ui.adsabs.harvard.edu/abs/2016AGUFMGC31D1142T

Tyler, R. H., 2017. Mathematical Modeling of Electrodynamics Near the Surface of Earth and Planetary Water Worlds. Technical Report TM-2017-219022, NASA.

https://ntrs.nasa.gov/citations/20170011279

Tyler, R. H., T. P. Boyer, T. Minami, M. M. Zweng, J. R. Reagan (2017), Electrical conductivity of the global ocean, *Earth, Planets and Space*, **69**:156, doi:10.1186/s40623-017-0739-7.

Tyler, R. H. (2021), A Century of Tidal Variability in the North Pacific Extracted From Hourly Geomagnetic Observatory Measurements at Honolulu, *Geophys Res Lett*, **48**.

UNESCO (1985), The international system of units (SI) in oceanography. *Technical Paper in Marine Science*, **45**, 124.

Wang, G., C. Zhao, M. Zhang, Y. Zhang, M. Lin, F. Qiao (2020), The causality from solar irradiation to ocean heat content detected via multi-scale Liang–Kleeman information flow. *Scientific Reports*, **10**, 17141; https://doi.org/10.1038/s41598-020-74331-2

Weaver, A. T., P. Courtier, (2001), Correlation modeling on a sphere using a generalized diffusion equation. *Q. J. Roy. Meteor. Soc.*, **127**, 1815–1846.

Wunsch, C., P. Heimbach, (2007), Practical global oceanic state estimation. *Physica D*, **230**, 197–208, https://doi.org/10.1016/j.physd.2006.09.040.

Wunsch, C., P. Heimbach (2013), Dynamically and kinematically consistent global ocean circulation and ice state estimates. Ocean Circulation and Climate, 2nd ed. G. Siedler et al., Eds., Elsevier.

Zika, J. D., J. M. Gregory, E. L. McDonagh, A. Marzocchi, L. Clément, 2021: Recent Water Mass Changes Reveal Mechanisms of Ocean Warming. *Journal of Climate*, *34*, 3461–3479; https://doi.org/10.1175/JCLI-D-20-0355.1.

Table 1. The area-weighted global averages of the pointwise temporal correlations between each of the electrical conductivity budget terms and the total tendency term, plus or minus the spatial standard deviation of the temporal correlations. Also listed are in parentheses are the (minimum, maximum) values of these temporal correlations.

budget term	correlation with total tendency term
Horiz adv T	-0.032 ± 0.10 (-0.60, 0.57)
Vert adv T	0.0062 ± 0.11 (-0.56, 0.66)
Horiz diff T	-0.0072 ± 0.11 (-0.82, 0.84)
Vert diff T	-0.061 ± 0.15 (-0.79, 0.53)
Forcing T	0.82 ± 0.35 (0.00070, 1.0)
Horiz adv S	0.014 ± 0.18 (-0.81, 0.90)
Vert adv S	-0.29 ± 0.22 (-0.99, 0.40)
Horiz diff S	0.015 ± 0.11 (-0.64, 0.74)
Vert diff S	-0.017 ± 0.092 (-0.69, 0.60)
Forcing S	0.0035 ± 0.037 (-0.50, 0.36)

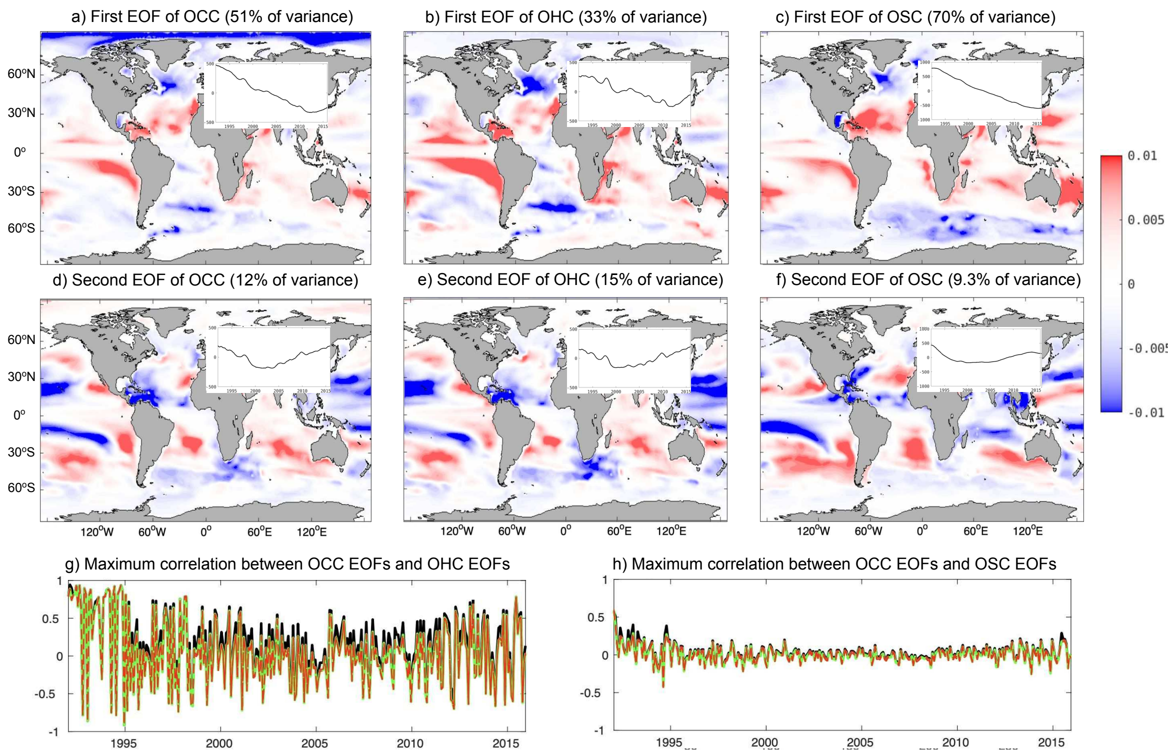

Figure 1. The first (panels a-c) and second (panels d-f) empirical orthogonal functions for area-weighted and normalized (scaled by standard deviations of) ocean conductivity content (OCC - panels a and d), ocean heat content (OHC - panels b and e), and ocean salt content (OSC - panels c and f). The inset time series over Eurasia are the corresponding Principal Components as a function of time. The units are dimensionless in panels a-f. Also shown are the maximum canonical spatial correlations (black curves) and maximum and minimum bootstrapped samples of spatial correlations (red dashed curves) around average spatial correlations (solid green curves) between the OCC EOFs and OHC EOFs as a function of EOF number (panel g) and between the OCC EOFs and OSC EOFs as a function of EOF number (panel h).

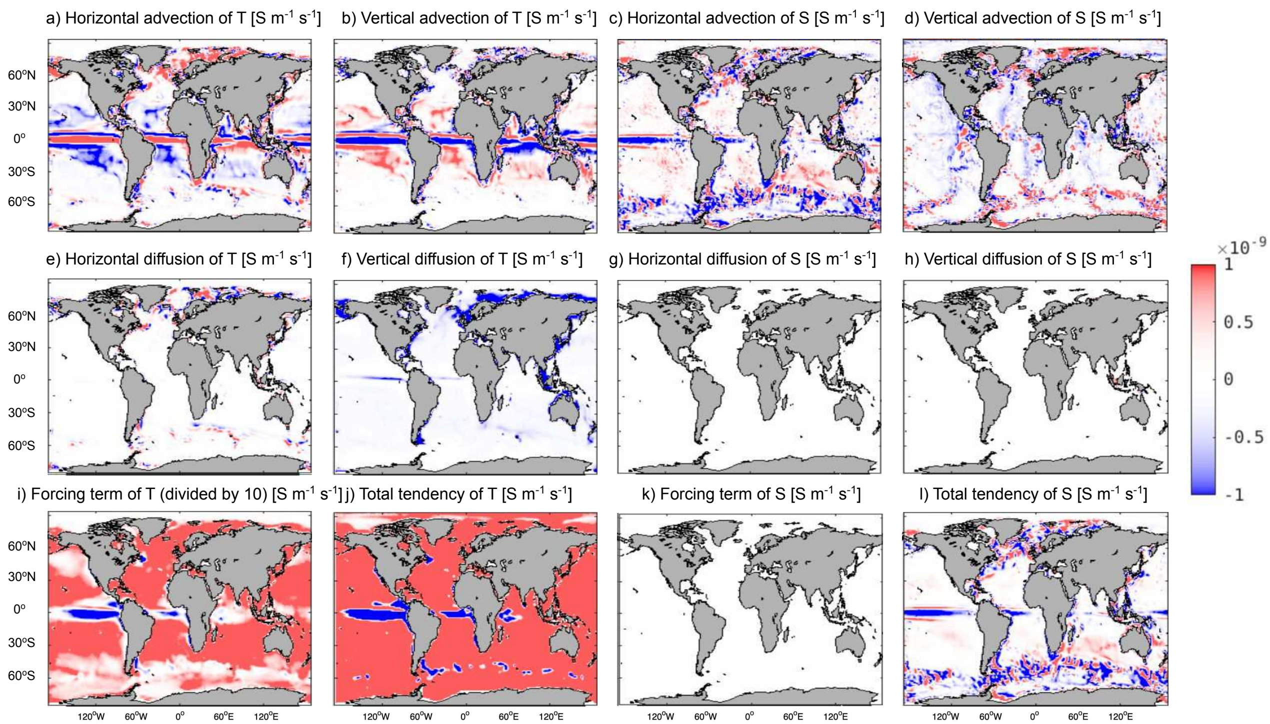

540 **Figure 2.** The depth-averaged electrical conductivity budget contributions (units in S m^{-1} s^{-1}) broken up into (a,c) horizontal advection, (b,d) vertical advection, (e,g) horizontal diffusion, (f,h) vertical diffusion, (i,k) forcing, and (j,l) total tendency terms for temperature (a-b, e-f, i-j) and salinity (c-d, g-h, k-l) terms. Note that the temperature forcing term has been divided by a factor of 10 to appear on the same colorbar scale as the other terms.

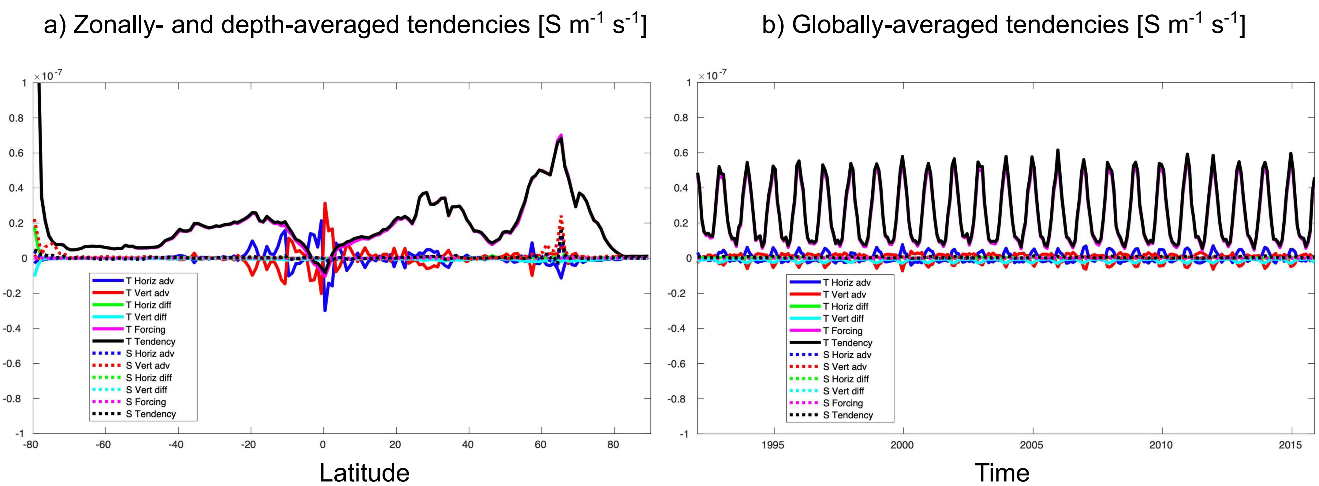

Figure 3. (Panel a) The zonally- and depth-averaged electrical conductivity budget contributions (units in S m^{-1} s^{-1}) broken up into horizontal advection (blue), vertical advection (red), horizontal diffusion (green), vertical diffusion (cyan), forcing (magenta), and total (black) tendency terms for temperature (solid) and salinity (dotted) terms and (panel b) the globally-averaged electrical conductivity budget contributions (units in S m^{-1} s^{-1}) broken up into the same tendency terms.

Figure 1.

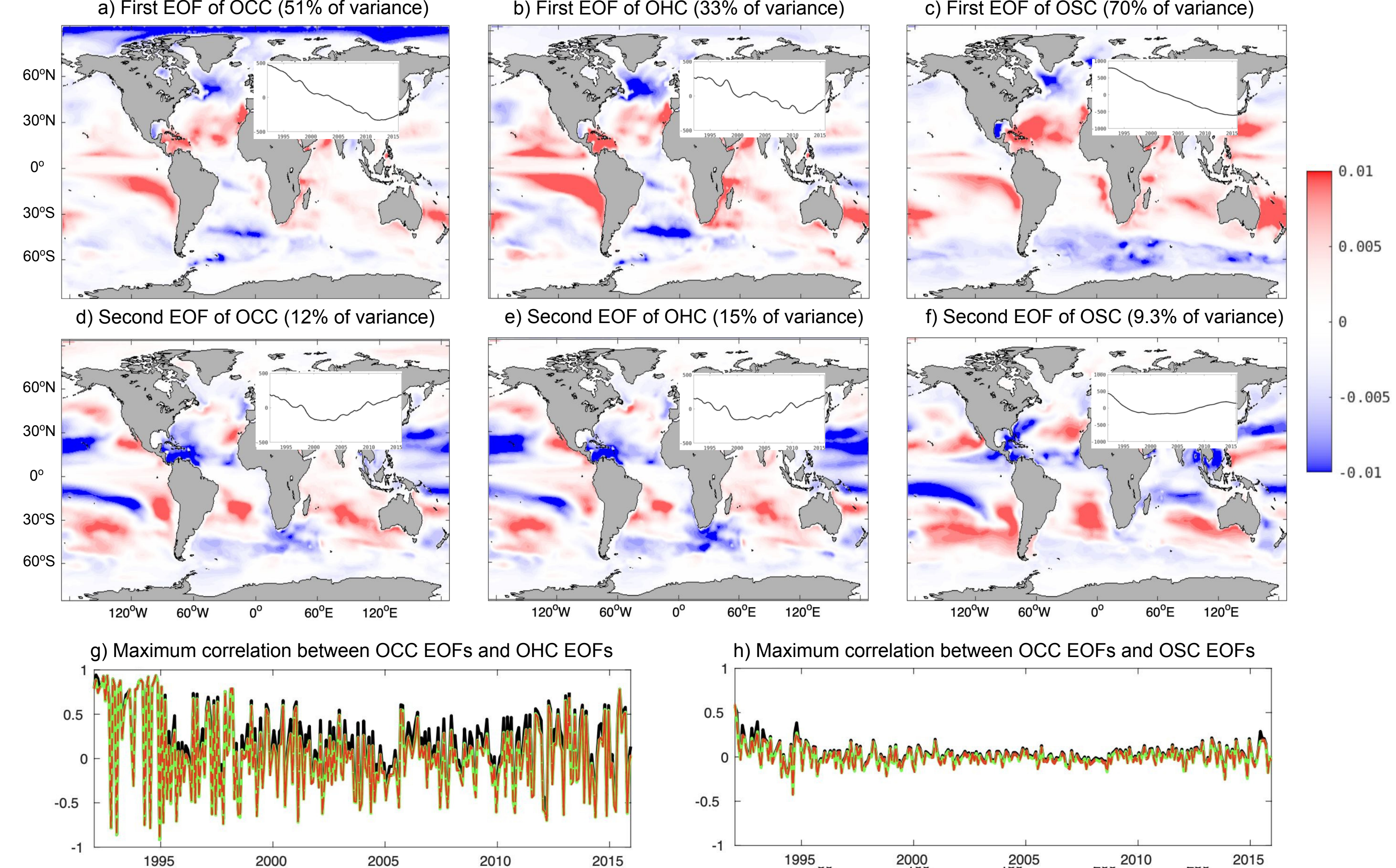

a) First EOF of OCC (51% of variance)
b) First EOF of OHC (33% of variance)
c) First EOF of OSC (70% of variance)
d) Second EOF of OCC (12% of variance)
e) Second EOF of OHC (15% of variance)
f) Second EOF of OSC (9.3% of variance)
60°N
30°N
0°
30°S
60°S
120°W
60°W
0°
60°E
120°E
0.01
0.005
0
-0.005
-0.01
g) Maximum correlation between OCC EOFs and OHC EOFs
h) Maximum correlation between OCC EOFs and OSC EOFs
1
0.5
0
-0.5
-1
1995
2000
2005
2010
2015

Figure 2.

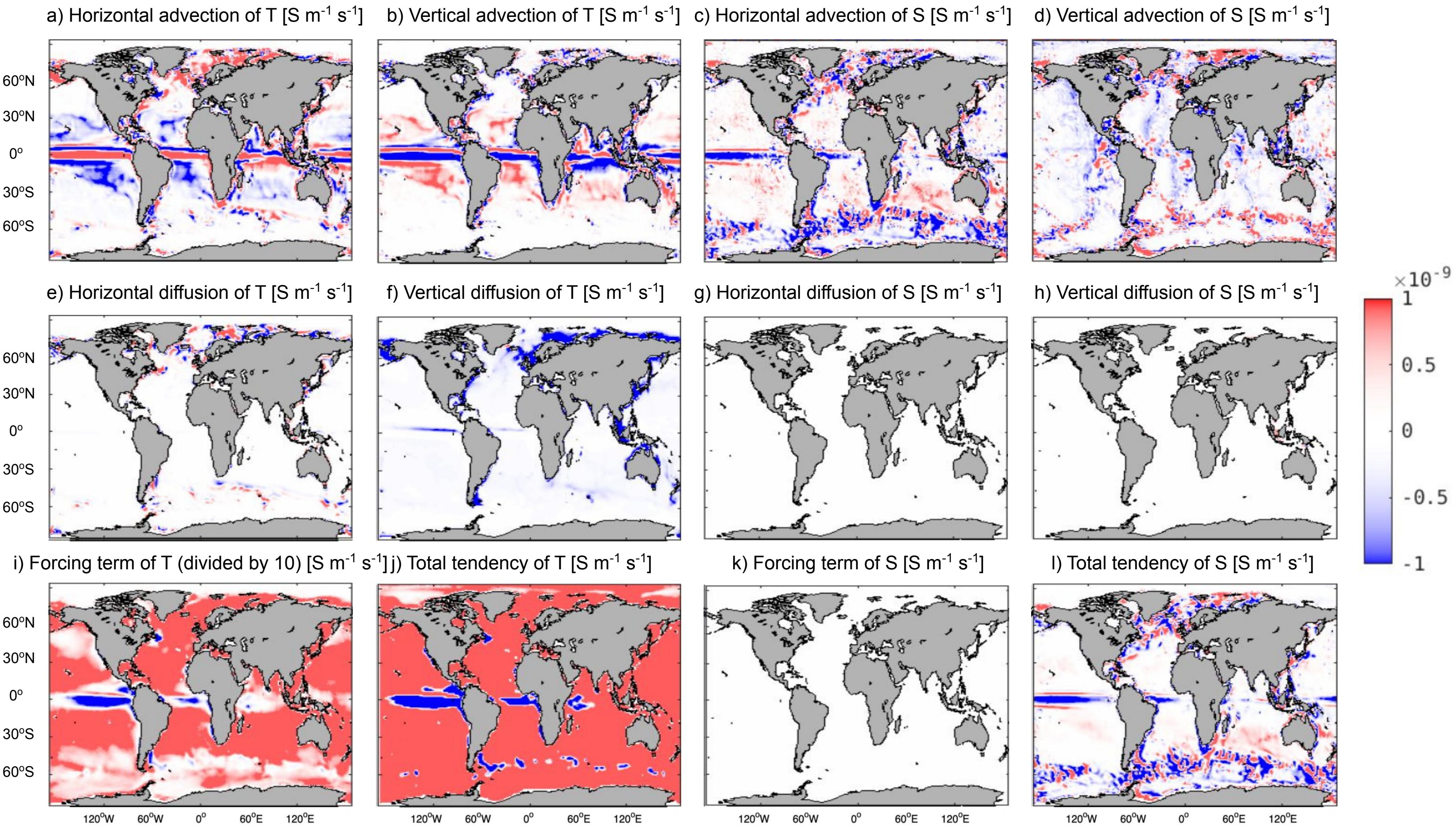
a) Horizontal advection of T [S m-1 s-1]
b) Vertical advection of T [S m-1 s-1]
c) Horizontal advection of S [S m-1 s-1]
d) Vertical advection of S [S m-1 s-1]
e) Horizontal diffusion of T [S m-1 s-1]
f) Vertical diffusion of T [S m-1 s-1]
g) Horizontal diffusion of S [S m-1 s-1]
h) Vertical diffusion of S [S m-1 s-1]
i) Forcing term of T (divided by 10) [S m-1 s-1]
j) Total tendency of T [S m-1 s-1]
k) Forcing term of S [S m-1 s-1]
l) Total tendency of S [S m-1 s-1]
60°N
30°N
0°
30°S
60°S
120°W
60°W
0°
60°E
120°E
×10-9
1
0.5
0
-0.5
-1

Figure 3.

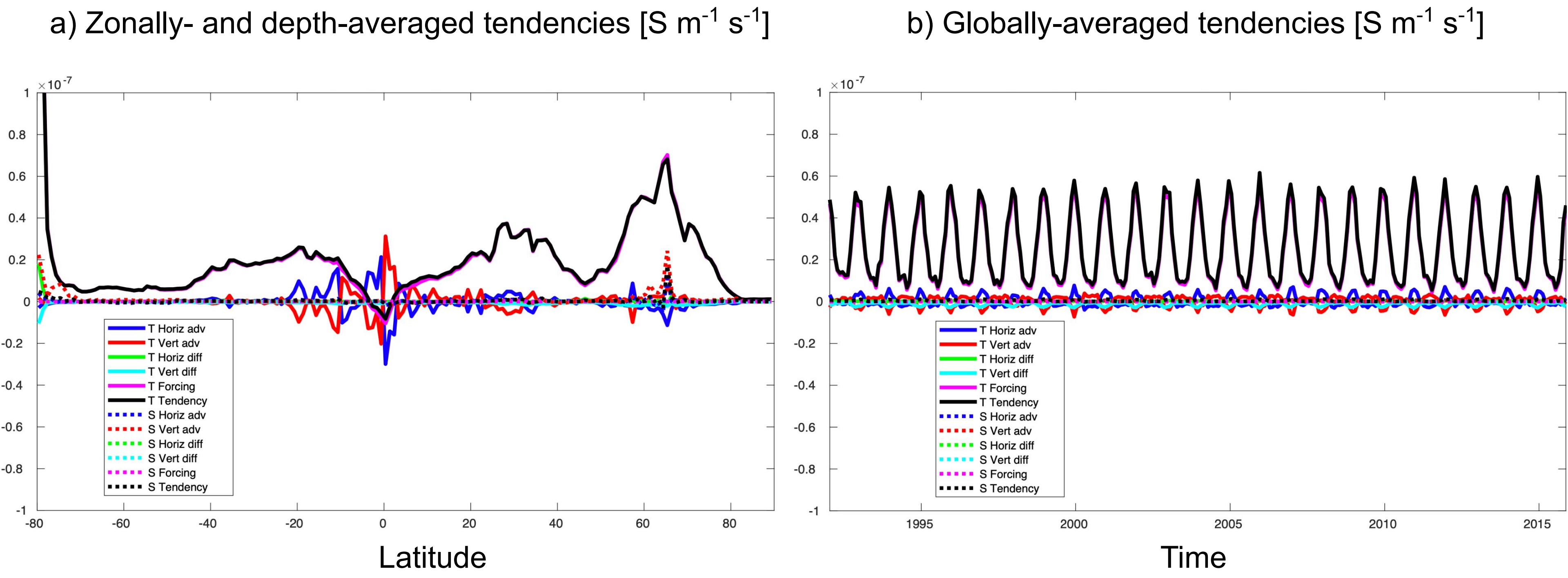
a) Zonally- and depth-averaged tendencies [S m-1 s-1]
b) Globally-averaged tendencies [S m-1 s-1]
×10-7
Latitude
Time
T Horiz adv
T Vert adv
T Horiz diff
T Vert diff
T Forcing
T Tendency
S Horiz adv
S Vert adv
S Horiz diff
S Vert diff
S Forcing
S Tendency

Figure S1.

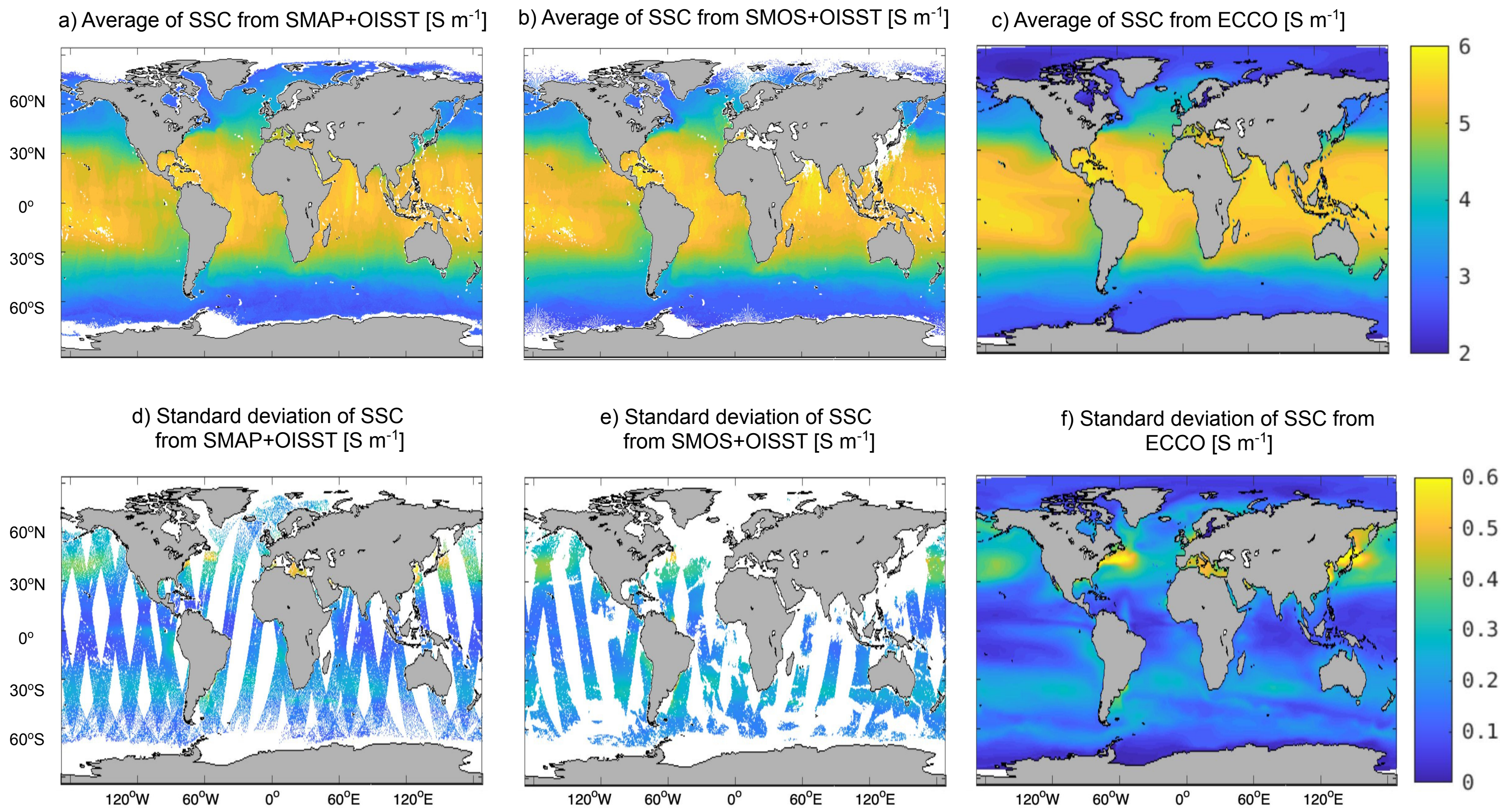
a) Average of SSC from SMAP+OISST [S m-1]
b) Average of SSC from SMOS+OISST [S m-1]
c) Average of SSC from ECCO [S m-1]
d) Standard deviation of SSC from SMAP+OISST [S m-1]
e) Standard deviation of SSC from SMOS+OISST [S m-1]
f) Standard deviation of SSC from ECCO [S m-1]
60°N
30°N
0°
30°S
60°S
120°W
60°W
0°
60°E
120°E
2
3
4
5
6
0
0.1
0.2
0.3
0.4
0.5
0.6

Figure S2.

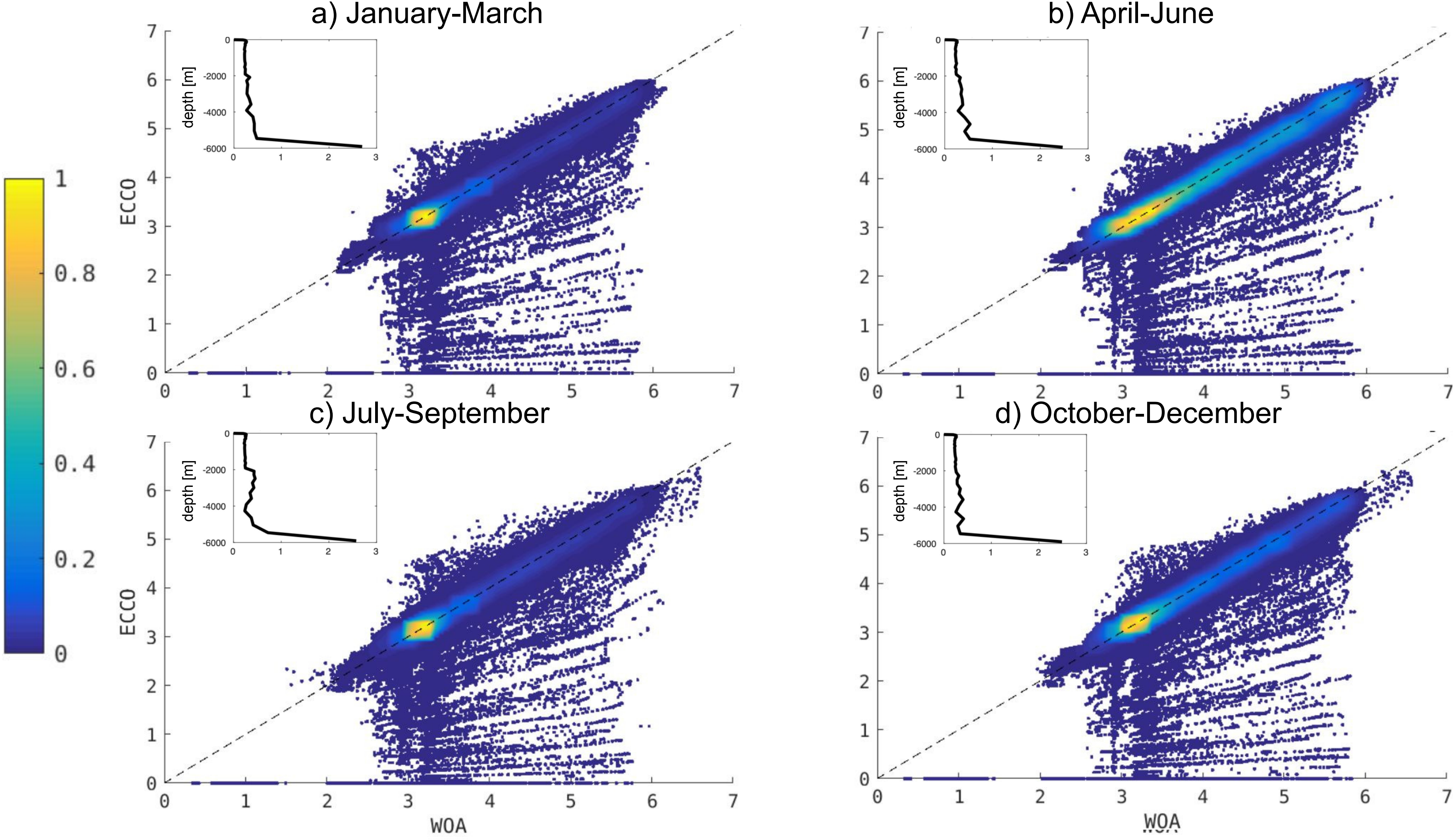

a) January-March
b) April-June
c) July-September
d) October-December
ECCO
WOA
depth [m]

Figure S3.

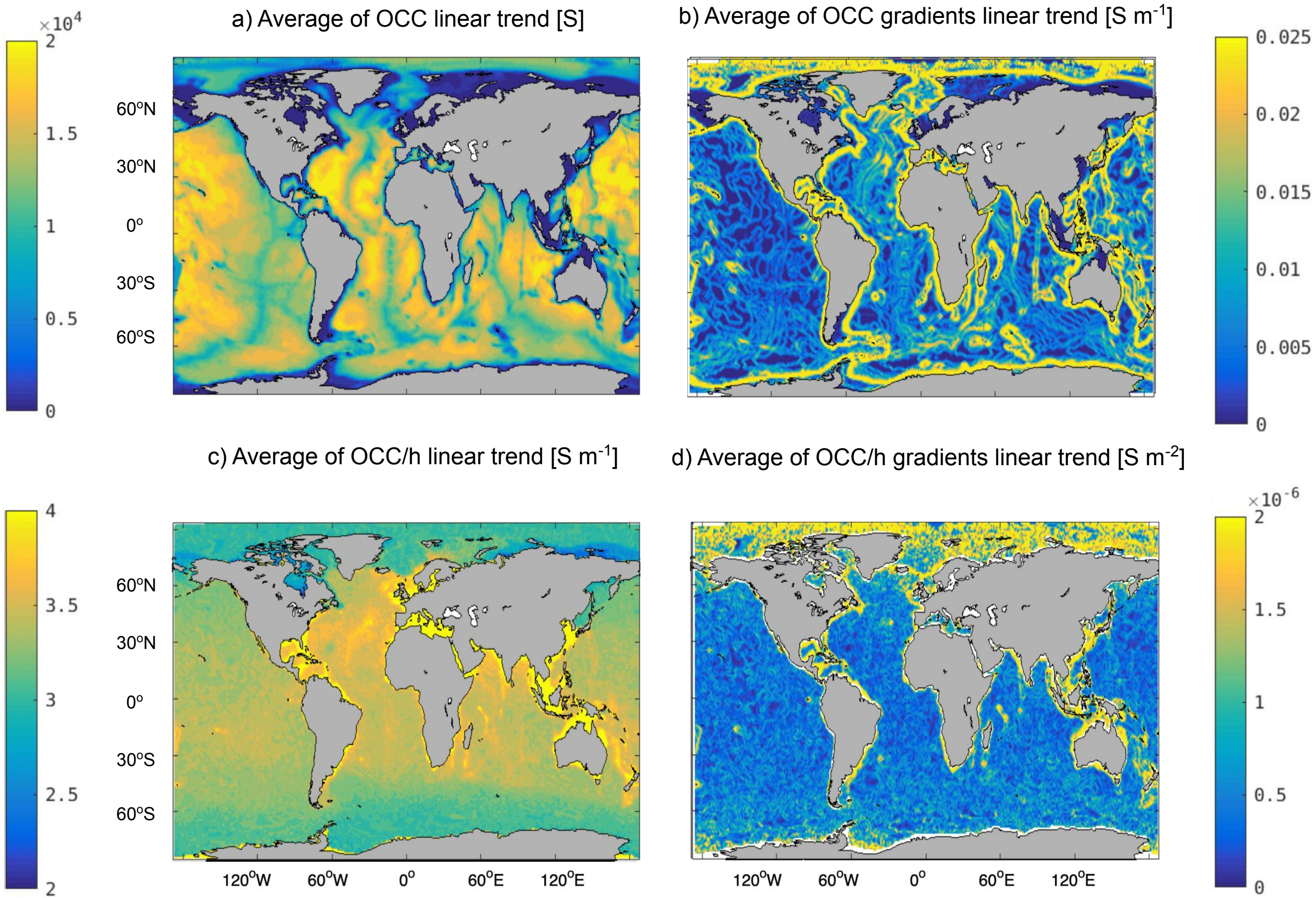

a) Average of OCC linear trend [S]
b) Average of OCC gradients linear trend [S m-1]
c) Average of OCC/h linear trend [S m-1]
d) Average of OCC/h gradients linear trend [S m-2]
×10^4
2
1.5
1
0.5
0
0.025
0.02
0.015
0.01
0.005
0
4
3.5
3
2.5
2
×10^-6
2
1.5
1
0.5
0
60°N
30°N
0°
30°S
60°S
120°W
60°W
0°
60°E
120°E

Figure S4.

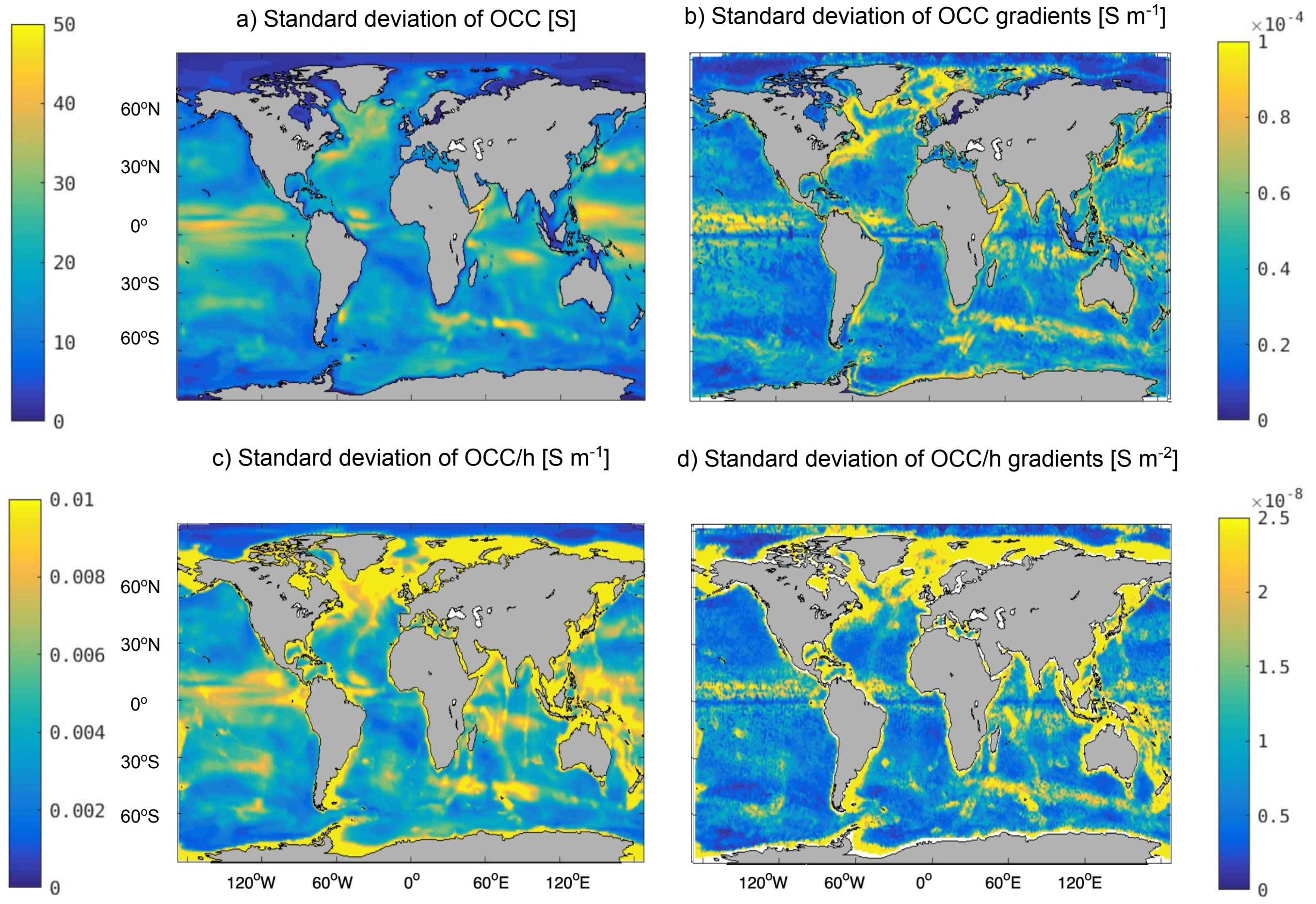

a) Standard deviation of OCC [S]
b) Standard deviation of OCC gradients [S m-1]
c) Standard deviation of OCC/h [S m-1]
d) Standard deviation of OCC/h gradients [S m-2]
50
40
30
20
10
0
×10-4
1
0.8
0.6
0.4
0.2
0
0.01
0.008
0.006
0.004
0.002
0
×10-8
2.5
2
1.5
1
0.5
0
60°N
30°N
0°
30°S
60°S
120°W
60°W
0°
60°E
120°E

Figure S5.

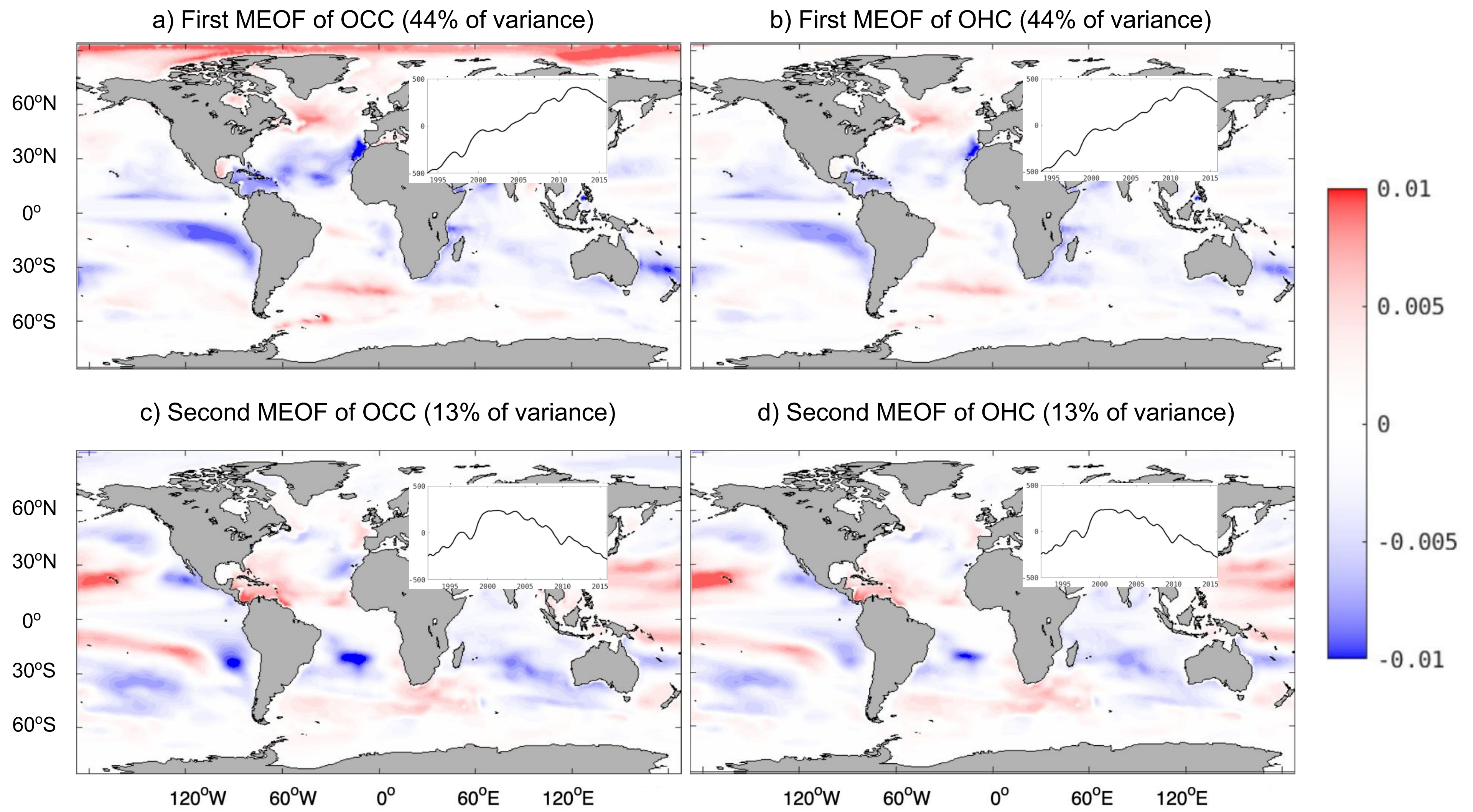
a) First MEOF of OCC (44% of variance)
b) First MEOF of OHC (44% of variance)
c) Second MEOF of OCC (13% of variance)
d) Second MEOF of OHC (13% of variance)
60°N
30°N
0°
30°S
60°S
120°W
60°W
0°
60°E
120°E
500
0
-500
1995
2000
2005
2010
2015
0.01
0.005
0
-0.005
-0.01

Supporting Information for "Electrical ocean conductivity variability from observations and its budget from an ocean state estimate"

D. S. Trossman,[1,2,3] R. H. Tyler[4,5]

Contents of this file

---

[1]Earth System Science Interdisciplinary Center, University of Maryland, College Park, MD, USA

[2]Department of Oceanography and Coastal Sciences, Louisiana State University, Baton Rouge, LA, USA

[3]Center for Computation & Technology, Louisiana State University, Baton Rouge, LA, USA

[4]Geodesy and Geophysics Laboratory, Code 61A, NASA Goddard Space Flight Center, Greenbelt, MD, USA

[5]Goddard Earth Science and Technology Research (GESTAR) II, University of Maryland, Baltimore County, MD, USA

4. Multivariate empirical orthogonal function (MEOF) analysis of ECCOv4r3

5. Figures S1-S5

Additional Supporting Information

1. Captions for Figures S1-S5

Observations for assessment of ECCOv4r3

We make use of the optimally interpolated sea surface temperature (OISST) combined with either the Jet Propulsion Laboratory's Soil Moisture Active Passive (SMAP) satellite mission Level-2 sea surface salinity (SSS) or the European Space Agency's Soil Moisture and Ocean Salinity (SMOS) mission Level-2 SSS data sets [*Reul et al.*, 2020] to calculate the sea surface conductivity (SSC). We require the OISST and either SMAP or SMOS data to be within 3.5 days and 50 km of each other to be considered simultaneous. We also mask out regions where the cold brightness temperature biases prevent us from retrieving reliable SSS data. These requirements prevents us from calculating an average or standard deviation of the SSC at every point where there are OISST data.

Because the ECCOv4r3 data are monthly, SMAP samples the same location every eight days, SMOS samples approximately the same location every eight days, and OISST is daily, we averaged the satellite-derived data over monthly time frames to compare its temporal variability with the same from model output. The ECCOv4r3 data have a longer time frame than the SMAP+OISST or SMOS+OISST time frames, so we only used 2010-2015 for ECCOv4r3; using the entire 1992-2015 time period isn't noticeably different. Such a short time frame doesn't allow us to distinguish temporal trends in the data and there are no visually distinguishable differences in the temporal standard deviations of the ECCOv4r3 data over 2010-2015 with or without detrending. Thus, we only remove the temporal mean (as opposed to trend) when computing the temporal standard deviations in the SSC.

We also make use of the climatological conductivity data described in the Introduction, specifically WOA18 *Reagan et al.* [2019]. The climatology conductivity data is not simply calculated from the temperature and salinity climatology data sets, as in *Manoj et al.* [2006] and *Grayver* [2021]. Rather, to retain thermodynamic consistency and also avoid known observational biases in the differently sampled temperature and salinity observations, the conductivity data is calculated only from co-sampled temperature and salinity observations. To perform a pointwise comparison of the WOA18 product with the ECCOv4r3 product, we calculate a seasonal climatology from the ECCOv4r3 output with the electrical conductivity computed in-line as the model runs and interpolate the WOA18 seasonal climatology data to the LLC90 grid.

Observational assessment of ECCOv4r3

Using the model output of the ECCO re-run, we compare the variability in electrical conductivity with that seen in observations. We first focus on the agreement between satellite-derived data and ECCOv4r3. Figure S1 shows qualitative and generally good quantitative agreement between the satellite-derived sea surface conductivity (SSC) and the ECCOv4r3-calculated surface layer conductivity. The average SSC is highest between 30^{o}S and 30^{o}N and lowest at high-latitudes in both the satellite-derived and ECCOv4r3-calculated fields, with their magnitudes very similar (Figs. S1a-c). The temporal standard deviation of SSC is highest in the vicinity of the Gulf Stream and Kuroshio Extension as well as in the Mediterranean Sea, Sea of Japan, and Sea of Okhotsk in ECCOv4r3 (Fig. S1f). These regions are poorly sampled in the satellite data, but to the extent these regions are sampled, the satellite data also find these regions to have the highest temporal variability (Figs. S1d-e). The satellite-derived data and ECCOv4r3 output agree that the regions with the lowest temporal variability are in both the low- and high-latitude regions (Figs. S1d-f). There is very high correlation between the satellite-derived data and ECCOv4r3 output (> 0.9) everywhere with sufficient satellite sampling.

We turn to assessing the agreement between the WOA seasonal conductivity climatology *Tyler et al.* [2017] and a seasonal climatology constructed from ECCOv4r3 output first presented in *Trossman and Tyler* [2019]. Figure S2 shows that the disagreements between the World Ocean Atlas (2018) and ECCOv4r3 products increase with depth, which is to be expected because of the relative dearth of observations with which ECCO is constrained at deeper depths. Over July-September, the contrast between < 2000 meters depth and > 2000 meters depth is particularly evident in the root-mean-square errors (RMSEs) because summer is the only season when northern high-latitude observations are taken, suggesting the disagreements below 2000 meters depth at northern high-latitudes are larger than elsewhere. The seasonal correlations are high in a globally averaged sense, but are highest (nearly perfect: > 0.98) at shallow depths in the open ocean and go down quickly to about 0.5 or less below about 700 meters depth (not shown). The disagreements are particularly evident at depths approaching 6000 meters depth because of the few constraints, even with ship-based hydrographic data. ECCO achieves relatively small values on continental shelves (particularly where is river outflow) and along some mid-ocean ridges (where geothermal heating is inadequately applied). However, electrical conductivities in ECCO are highly consistent with observations in the vast majority of the ocean.

Temporal variability of OCC and its spatial gradients in ECCOv4r3

We assess the temporal variability in OCC and its horizontal spatial gradients over the entire length of the ECCOv4r3 product (1992-2015). We first remove the averages of the OCC (Fig. S3a), its horizontal spatial gradients (Fig. S3b), and depth-averaged equivalents (Figs. S3c-d), estimated with a best fit via linear regression, before computing the temporal standard deviations of each quantity. The averages of the OCC and its depth-average are very similar to the climatology constructed by *Tyler et al.* [2017] (see their Figure 2). The horizontal spatial gradients in OCC and its depth-average are largest near the coasts and in the Arctic Ocean, with a wealth of fine-scale spatial variability. This is important as these gradients appear in the equations governing ocean electrodynamics. The temporal standard deviations of the linearly detrended OCC (Fig. S4a) are largest in regions with the largest air-sea fluxes. Without detrending, the standard deviations of OCC (not shown) look almost identical to the standard deviations of the sea surface conductivity (Fig. S1f), suggesting that the majority of the variability in OCC occurs near the surface. This is consistent with the findings of *Irrgang et al.* [2018]. The standard deviations of the horizontal gradients in OCC (Fig. S4b) tend to be largest in regions with the steepest topographic slopes as well as in some equatorial regions. The standard deviations of the depth-averaged conductivity (Fig. S4c) are largest on continental shelves and next-largest over mid-ocean ridges because of higher surface variability and their relatively shallow depths, indicating that the seafloor depths primarily determine the spatial pattern. The standard deviations of the horizontal gradients in OCC divided by the seafloor depth h (Fig. S4d) attain their largest values in regions with the largest topographic slopes, demonstrating that their spatial pattern is again primarily set by the seafloor depths. While the near-surface variability clearly plays an important role in setting the variability in OCC and the horizontal gradients in OCC, how the variability in OCC relates to that in OHC needs to be better understood, which we investigate next.

Multivariate empirical orthogonal function (MEOF) analysis of ECCOv4r3

We apply a multivariate empirical orthogonal function (MEOF) analysis of OCC and OHC to assess their spatial patterns of covariability. We remove the temporal means of the OCC and OHC fields, area-weight each field, and normalize them by their standard deviations prior to calculating the MEOFs, as we did with the EOF analyses shown in Fig. 1. The MEOF analysis suggests the first MEOF (Figs. S5a-b) explains about the same percent of the (co)variance (between one-third and one-half) as our EOF analyses shown in the main text (Figs. 1a-b). The second MEOF for OCC and OHC are related to natural climate variability (Figs. S5c-d) and explains about the same percent of the (co)variance (10-15%) as our EOF analyses shown in the main text (Figs. 1d-e). The MEOF spatial patterns shown in Fig. S5 are visually identical to those shown in Figs. 1a-b and 1d-e, apart from their sign.

References

Grayver, A. V. (2021), Global 3-D electrical conductivity model of the world ocean and marine sediments, *Geochemistry, Geophysics, Geosystems*, **22**, e2021GC009950, https://doi.org/10.1029/2021GC009950

Irrgang, C., J. Saynisch-Wagner, M. Thomas (2018), Depth of origin of ocean-circulation-induced magnetic signals, *Ann. Geophys.*, **36**, 167–180, https://doi.org/10.5194/angeo-36-167-2018

Manoj, C., A. Kuvshinov, S. Maus, H. Luhr, (2006), Ocean circulation generated magnetic signals. *Earth, Planets and Space*, **58**(4), 429–437.

Reagan, J.R., M.M. Zweng, D. Seidov, T.P. Boyer, R.A. Locarnini, A.V. Mishonov, O.K. Baranova, H.E. Garcia, K.W. Weathers, C.R. Paver, I.V. Smolyar, R.H. Tyler (2019). World Ocean Atlas 2018, Volume 6: Conductivity. A. Mishonov Technical Editor, NOAA Atlas NESDIS 86, 38 pp.

Reul, N., S. A. Grodsky, M. Arias, J. Boutin, R. Catany, B. Chapron, F. D'Amico, E. Dinnat, C. Donlon, A. Fore, et al., 2020: Sea surface salinity estimates from spaceborne L-band radiometers: An overview of the first decade of observation (2010–2019). *Remote Sens. Environ.*, **242**, 111769.

Trossman, D. S., R. H. Tyler, 2019: Predictability of Ocean Heat Content from Electrical OCC. *Journal of Geophysical Research-Oceans*, **124**, 667-679; https://doi.org/10.1029/2018JC014740.

Tyler, R. H., T. P. Boyer, T. Minami, M. M. Zweng, J. R. Reagan (2017), Electrical conductivity of the global ocean, *Earth, Planets and Space*, **69**:156, doi:10.1186/s40623-017-0739-7.

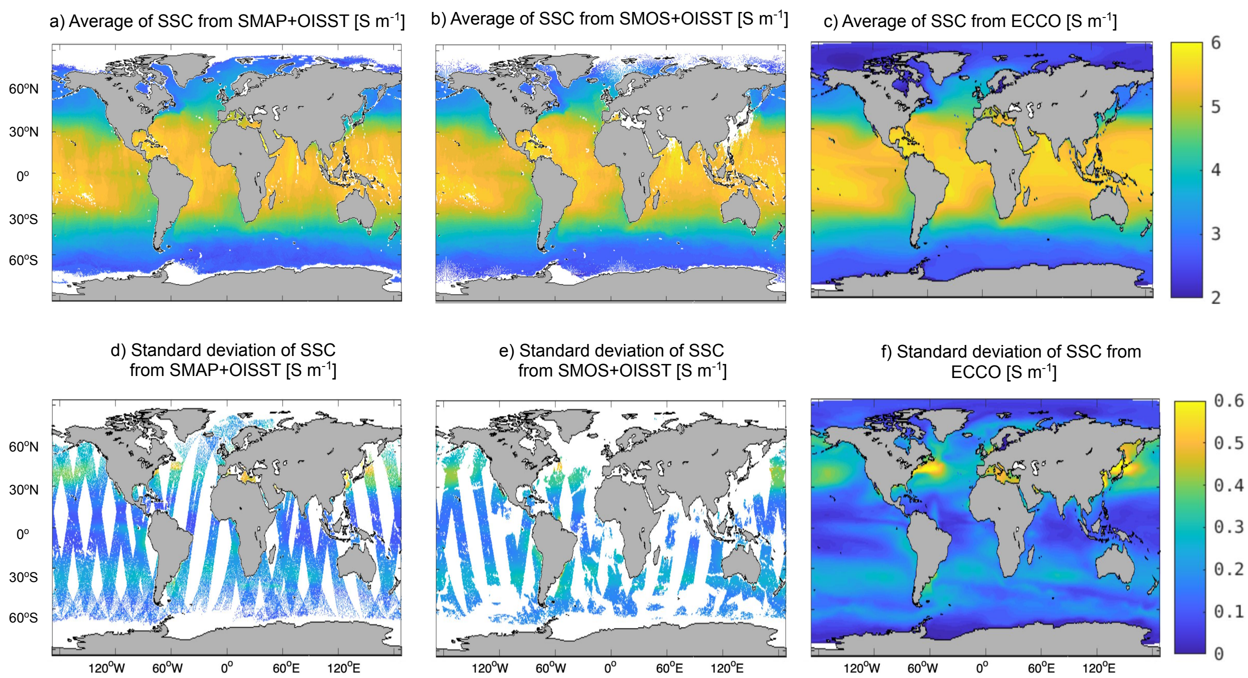

Figure S1. The average sea surface conductivity (SSC [units in S m^{-1}]) (panels a-c) and standard deviation of SSC (panels d-f) over the length of the SMAP mission (April of 2015 through 2021 - panels a and d), over the length of the SMOS mission (June of 2010 through 2021 - panels b and e), and over the length of the ECCOv4r3 product (January of 1992 through 2015 - panels c and f).

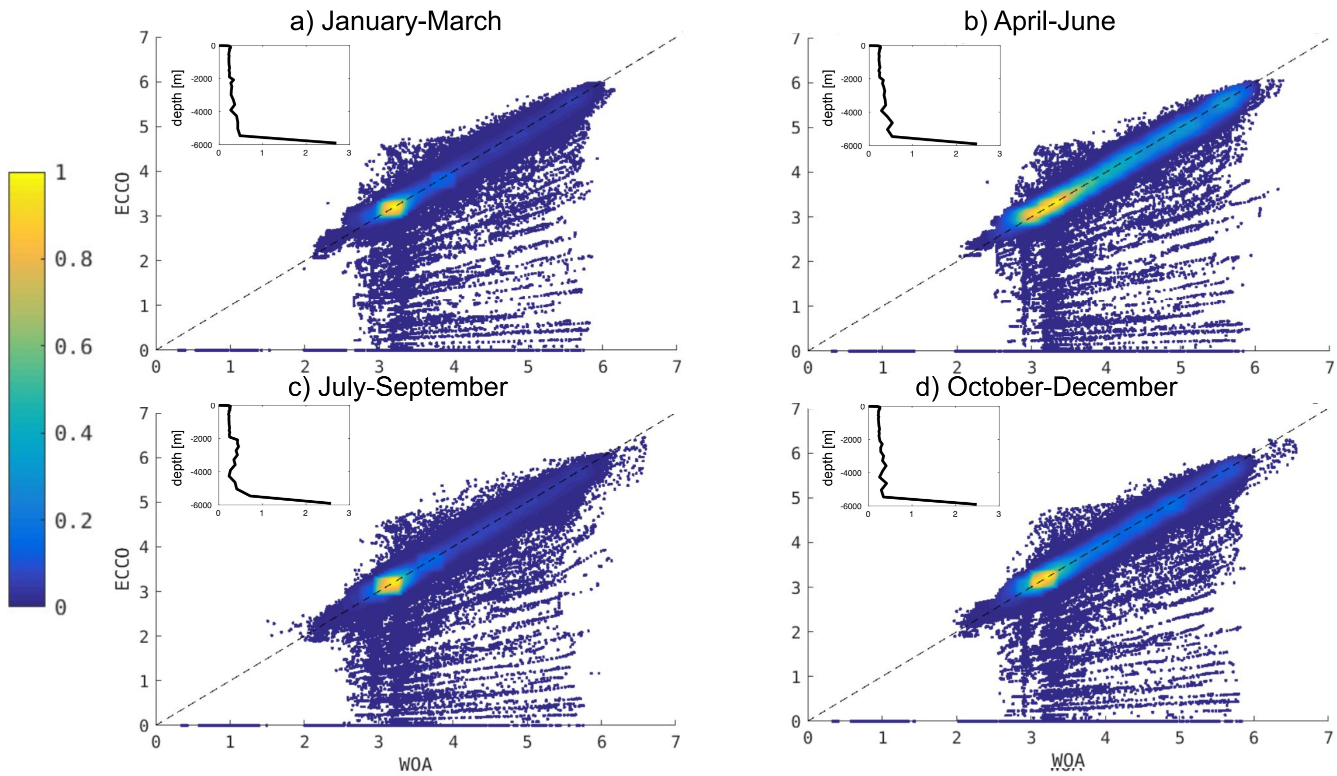

Figure S2. The depth-averaged electrical conductivity from the World Ocean Atlas (2018) or WOA (abscissa) and ECCOv4r3 (ordinate) seasonal climatologies from January-March (panel a), April-June (panel b), July-September (panel c), and October-December (panel d). The inset profiles in each panel indicate the root-mean-square error (RMSE) between the WOA and ECCOv4r3 products as a function of depth.

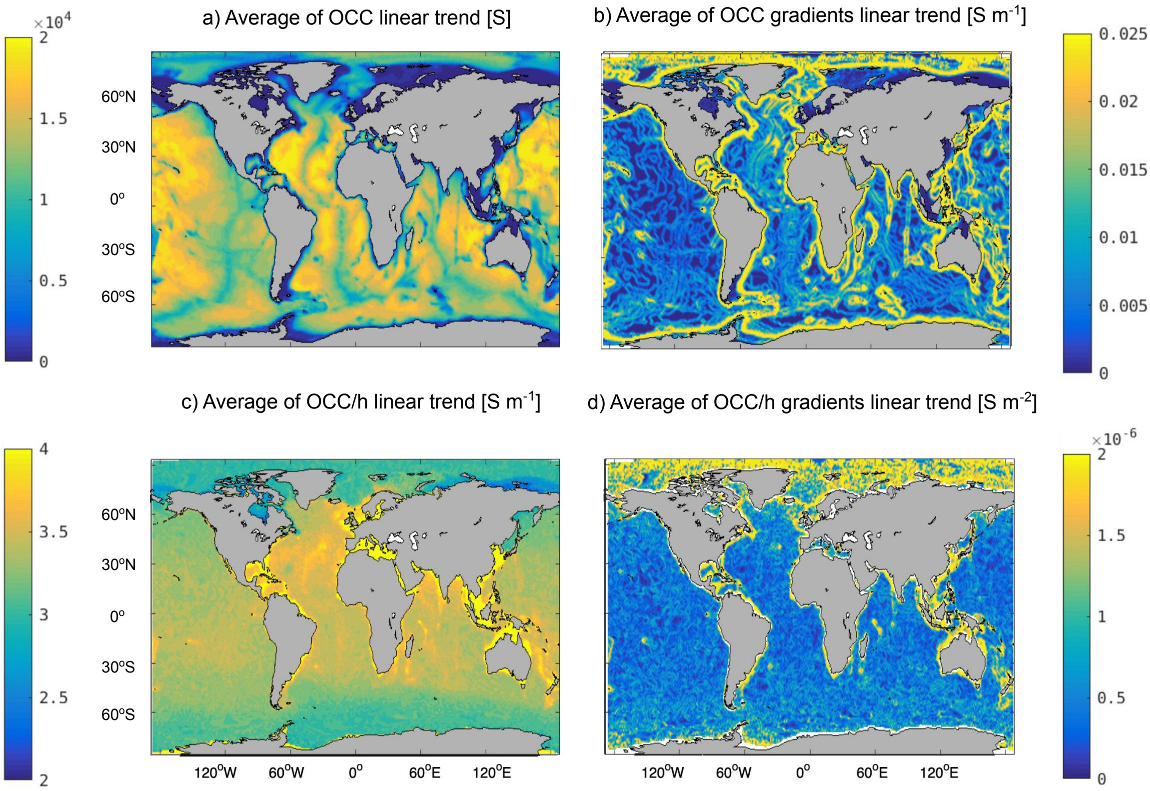

Figure S3. The temporal averages of the linear regression-based predictions for the ocean conductivity content (OCC) (panel a; units in S); horizontal gradients in OCC (b; units in S m^{-1}); depth-averaged electrical conductivity (OCC/h) (c; units in S m^{-1}), and the horizontal gradients in OCC divided by the seafloor depth (d; units in S m^{-2}) from ECCOv4r3.

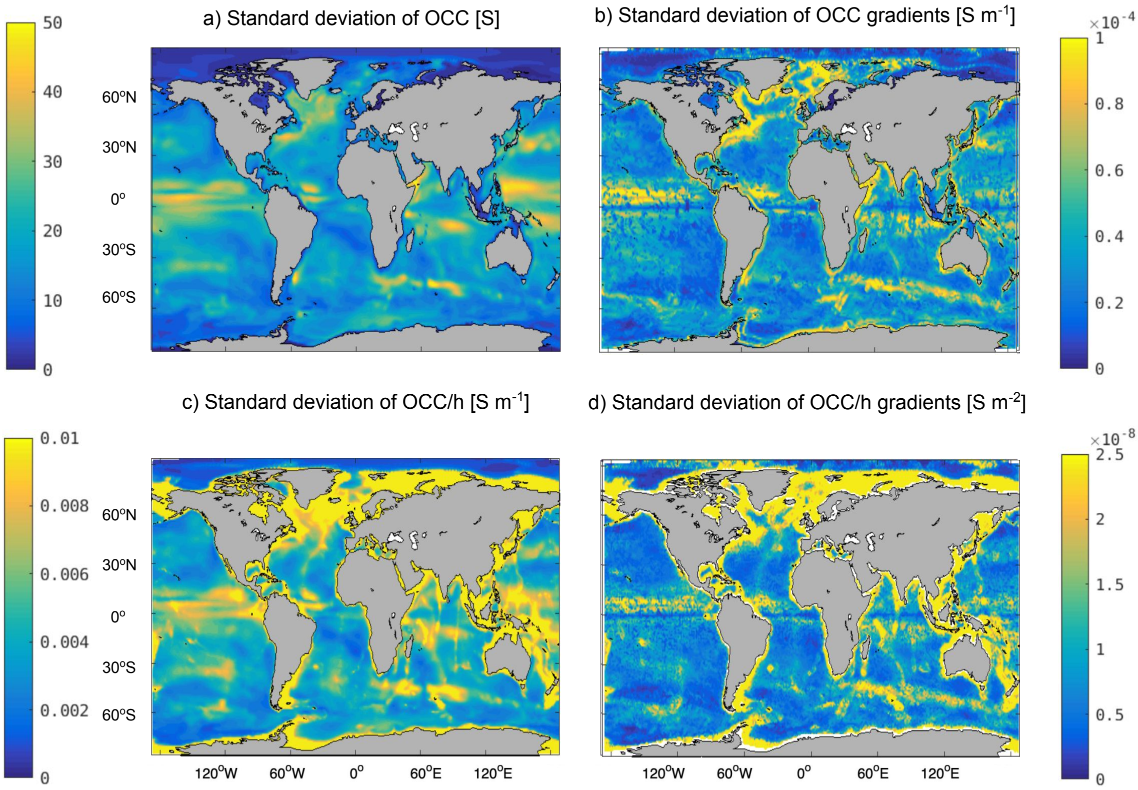

Figure S4. The temporal standard deviations of the ocean conductivity content (OCC) (panel a; units in S); horizontal gradients in OCC (b; units in S m^{-1}); depth-averaged electrical conductivity (OCC/h) (c; units in S m^{-1}), and the horizontal gradients in OCC divided by the seafloor depth (d; units in S m^{-2}) from ECCOv4r3.

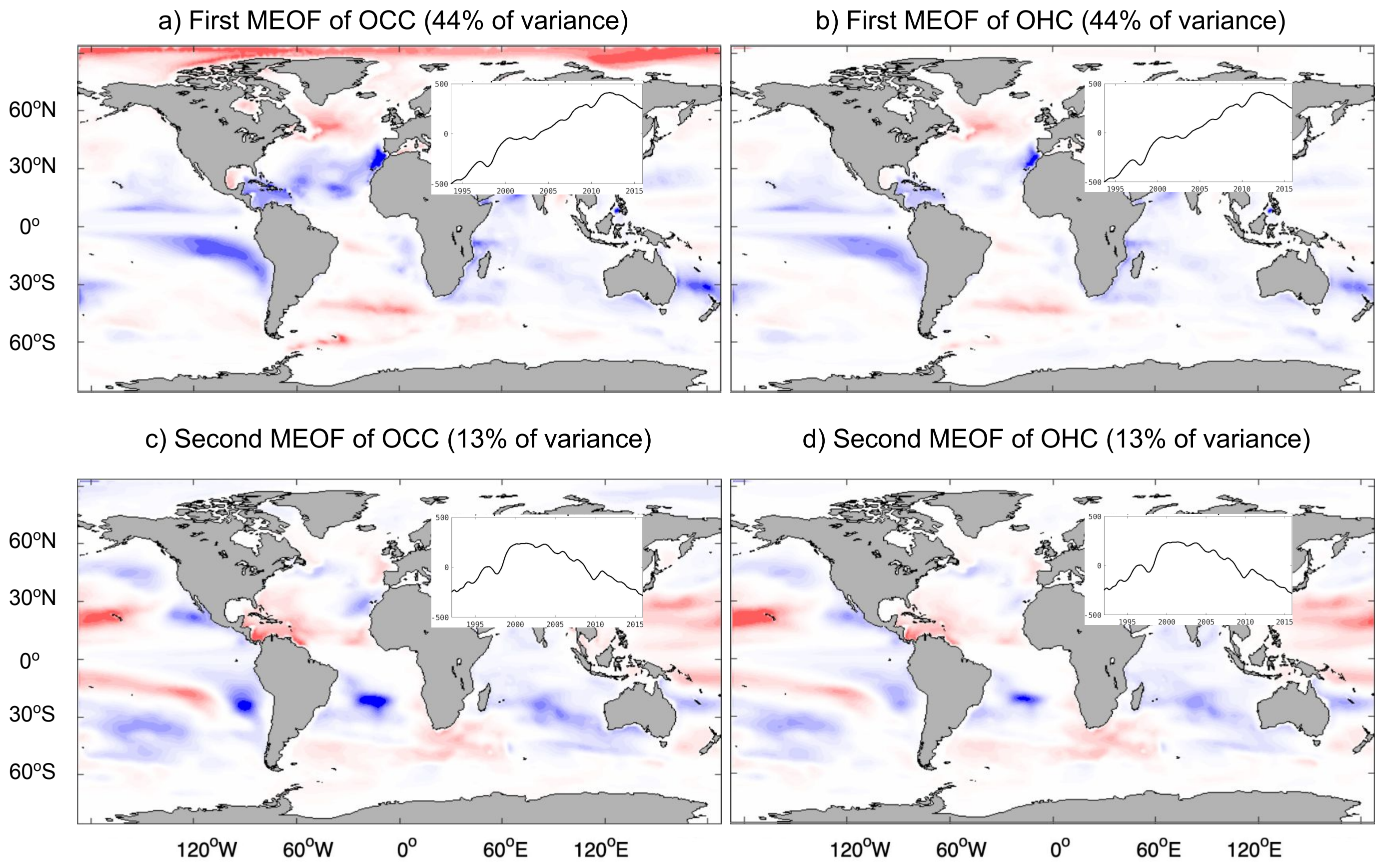

Figure S5. The first (panels a-b) and second (panels c-d) multivariate empirical orthogonal functions for area-weighted and normalized (scaled by standard deviations of) ocean conductivity content (OCC) and ocean heat content (OHC) from ECCOv4r3. The inset time series over Eurasia are the corresponding Principal Components as a function of time. The units are dimensionless for each panel.